Assessment of turnout crossing degradation

Using in-service passenger train axle box accelerations

B. Bogojević

TU Delft

ProRail

Assessment of turnout crossing degradation

Using in-service passenger train axle box accelerations

by

B. Bogojević

to obtain the degree of Master of Science
at the Delft University of Technology,
to be defended publicly on the 26th of May 2023 at 14:30.

Student number:	4299183		
Project duration:	March 2022 – May 2023		
Thesis committee:	Dr. V.L. Markine	TU Delft	chair
	Prof. Dr. Ir. R.P.B.J. Dollevoet	TU Delft	supervisor
	Dr. F. Kavoura	TU Delft	supervisor
	Ir. J.J.J. Wegdam	ProRail	daily supervisor

Cover: Vossloh Cogifer 1/15 UIC60 fixed crossing located near Murjek, Sweden.

TU Delft ProRail

Preface

After a long period of not only studying, I actually may call myself an engineer. Although I am by far not the only one reaching this milestone, I am absolutely proud of carrying this title, granted by the TU Delft. Nature is truly incredible and I consider engineering as the fascinating craftsmanship of tweaking nature to benefit from its capabilities. There is something special about gaining knowledge and useful insights in many fields or disciplines. Something I enjoyed so much, it did not bothering me to hurry or stick to the predefined study pace. It gave me the inglorious title of eternal student among friends.

However, being the eternal student made me to not only listen to professors and study the books. I joined committees at study associations and I am grateful that I got the chance to lead the amazing student association U-BASE as chairman for a year. I was able to dig into topics related to computers, programming and networking which always fascinated me as a child. As student-assistant of the section of Railway Engineering I've been able to help and learn from many field measurements in The Netherlands, Romania and Sweden. Some of which as part of European research projects. There are not many opportunities like this, and I am grateful to have been part of this. I would like to thank all colleagues from the section of Railway Engineering for these unique educational experiences. A special thanks to Jan and Jurjen for the seamless teamwork and fun during many of these trips.

Something I am particularly proud of is realising my childhood dream by becoming the youngest bus driver at the time. Next to studying, I've been driving many groups of people of which some I knew well on trips I sometimes organised myself. The first lockdown due to the COVID-19 pandemic made me realise my second childhood dream, becoming a truck driver. Looking back, it feels surrealistic that streets were absolutely deserted, I had a permit to be outside and truck drivers driving food were considered hero's for a while. The lockdown and heroism ended, my passion certainly did not.

This work symbolises an incredible fun and happy period in life for me. I owe a huge thank you to the people I may call my friends and family, that were part of this period. In no particular order: my sisters Myrthe and Relinde, brother Finn, stepfather Hans, my always hospitable Serbian family, A63 housemates, Jaarbeien, Eldin, 6V, #Docking. I just realised that after finishing the BSc, there were not many courses, assignments, committees or boards where I have not been teaming up with you, Dennis. Besides forming a good team, I enjoyed the countless party's, beers, whisky's, meals and chats we had. Thanks for the great teamwork and making the Master so much fun! Heleen, you deserve a special mention. I absolutely admire your endless positivity. Thank you for your love, especially since I have not always been easy on you.

I would like to thank my graduation committee for their supervision. A special thank you to Valeri for the informal meetings, in and outdoors, at noon or night. Jeroen, you absolutely rock as daily supervisor. I consider myself lucky to had such a helpful, fun and like-minded supervisor. Thank you for the great supervision, during and after working hours. I also would like to thank colleagues from ProRail Ivan for taking me on nightly on-site inspections and Theo for the unofficial, but very helpful and welcome supervision. The lost working hours due to the sparking discussions about the future of railway monitoring were absolutely worth it.

Before finalising, I would like to thank opa Hans and oma Helen for being such loving and caring people, always encouraging and supporting me to study. The thought of oma not being able to see me graduate makes me sad, but the happy memories from her I cherish counter that.

In my final words, I would like to express my gratitude towards my mother Margreet and father Goran. Not only because you are the best parents a child could wish for, but also for giving me the opportunity to study, providing unconditional support and always believe in me. I love you, I have an eternal debt to you.

B. Bogojević
Delft, May 2023

Summary

Turnouts introduce flexibility into railway networks but are relative sensitive railway components. Rising demand for capacity, higher speeds, higher axle loads and less time for maintenance pressures the reliability of turnouts. Especially a fixed crossing that facilitates the physical intersection of two rails is vulnerable. It contains a discontinuity that causes large impact forces potentially leading to an abrupt failure and large disruptions. This gives rise to the question if failures and the following disruptions can be prevented or mitigated by timely maintenance. Early detection is at the base of preventive (fix small problems before they become big ones) or predictive maintenance (estimate health degradation and act accordingly), requiring small monitoring intervals. Passenger trains cover a large extend of the Dutch network at a daily basis and therefore they can serve as a platform for frequent infrastructure monitoring. A potential infrastructure monitoring technology that is applicable to retrofit is on passenger trains is Axle Box Accelerations. By having two intercity trains of NS retrofitted with this system, the objective of this thesis is to develop an assessment method to determine the crossing health. This can be translated into the main research question ”How can in-service passenger train Axle Box Accelerations (ABA) be utilised to assess the structural health of a turnout crossing?”.

The wing rails and a crossing nose together form the crossing. Together, they provide the physical intersection of two rails. The wheel-rail contact transitions where the crossing nose and wing rail level. This discontinuity disturbs the wheel motion and thereby it forms an excitation in the train-track interaction at the crossings in the form of impact forces. In general, high impact forces are the leading causes of defects, wear, and failure of other railway components and should therefore be kept to a minimum. Plastic deformation and/or RCF are two degradation mechanisms that are linked to the magnitude of impact forces. Wear is another degradation mechanism that is mainly dominated by relative velocities between wheel and rail, which is most often during flange-rail contact (irregular contact). Therefore, by impact forces and irregular contact the condition of a crossing nose could be assessed.

The axle box is the stationary point closest to the wheel-rail interface. Therefore, the accelerations (and thus forces) originating from the wheel-rail interface is reflected in the Axle Box Accelerations (ABA) measurements. In this thesis, ABA measurements from two intercity trains of NS are considered. In-service passenger trains cover a large extent of the railway network and often multiple times a day. This makes in-service passenger trains a good candidate for this monitoring system, yielding information about the track state with small time intervals. However, this also introduces challenges with respect to data quality, quantity and processing. Furthermore, uncertainties are introduced since the measurements are conducted at random from the IM perspective, under random conditions (e.g. speed, loading, etc). The current measurement setup causes at low sampling frequency yields less accurate results for crossing health determination. This is shown by a reconstruction of the processing based on high-frequency measurements conducted by another vehicle at the same crossing. As a consequence, the low sampling frequency requires to deviate from previous conducted studies where time-frequency analysis yield promising results. A statistical approach can overcome the frequency limited measurements. The Law of Large Numbers, supplemented by the Central Limit Theorem can leverage the strong features of the system: large amount of measurements with relative small intervals.

The vertical impact and impact angle distribution are the features of a single crossing that are taken into consideration. The proposed assessment is based on the two characteristics that describe a normal distribution: the mean and standard deviation. By means of a correlation analysis, the method is validated against geometry metrics derived from train-borne laser measurements. The impact angle features were expected to be related to wear levels on the crossing nose and wing rail. Based on geometry laser measurements wear levels were determined. The wear generated during the ABA measurement period specifically is also considered. However, the current approach does not yield any (reliable) relationship between the impact angle and wear levels. Therefore, the current approach is not suitable for monitoring wear levels of crossings. A strong relationship between the kinematic wheel dip angle and mean vertical impact was found. Heavily degraded crossings are found in case studies for the largest impact means, stipulating this relationship. The vertical geometry can therefore be assessed, where a larger mean indicates a more degraded vertical geometry.

Contents

List of abbreviations

ABA	Axle Box Accelerations	ii, 2, 3, 13, 17, 23, 25, 30, 31, 34, 37, 38, 41
ADC	Analog to Digital Converter	14–17
API	Application Programming Interface	38
BW	Bandwidth	15
CTO	Centrum Technologisch Onderzoek (TU Delft's measurement vehicle)	13, 16–19
FS	Full Scale	15
IM	Infrastructure Manager	ii, 1, 2, 12, 13, 21, 23
LSB	Least Significant Bit	15
MBS	Multi-Body System	6, 41
MEMS	Microelectromechanical System	14
MPU	Main Processing Unit	14
NS	Nederlandse Spoorwegen (Dutch Railways)	2, 13
ODR	Output Data Rate	15
PWMD	Peripheral Wireless Measurement Device	14
RaM	Reizigerstrein als Meettrein (passenger train as measurement train)	2, 13, 16–19, 23
RCF	Rolling Contact Fatigue	2, 9, 10, 12, 37
S&C	Switches and Crossings	1, 2, 4
SF	Sampling Frequency	15, 16, 19, 23, 31, 38
SHM	Structural Health Monitoring	1, 2, 11, 12, 23
SNR	Signal to Noise Ratio	16, 18
TP	Theoretical Point (located at the tip of a Dutch crossing nose)	5, 41

1

Introduction

1.1. Motivation

1.1.1. Newspaper headlines

It is not very common to see national newspaper headlines related to railway defects directly. Operational performance or a severe derailing is more likely to be reported. However, on the verge of the evening rush hour on Monday August 8th 2022, while writing this thesis, the Dutch national news was dominated by a railway defect. During a manual ultrasonic inspection, a ruptured crossing nose was found close to a major junction (Leiden). As per regulation, all traffic was suspended over this turnout until the crossing nose is renewed. Unfortunately, this particular turnout is part of a main line (Leiden-Schiphol) and could not be bypassed. To make matters worse, there was an already malfunctioning turnout on a parallel main line (the feasible alternative route) causing suspended services. Eventually this triggered a cascade of cancelled services on many main lines in the whole country. On the very few services that were not directly impacted by the defect, there were extreme delays and overcrowded platforms and trains due to the overflow of diverted travellers. Many travellers did not reach their destination by train this evening. The impact of such a sudden failure shows how vital the state of a single crossing can be. These kind of sudden failures causing large disruptions give rise to the question if the failure could have been prevented or mitigated.

1.1.2. Current monitoring of turnouts

Prevention or mitigation of structural problems starts with detection. This is the field of Structural Health Monitoring (SHM), also known as condition monitoring. SHM gives insight in the current status and performance of infrastructure. It enables IM's and contractors to act timely and perform maintenance based on the actual state of the infrastructure. The Dutch railway IM ProRail currently monitors the structural health of turnouts by utilising dedicated measurement trains that measure turnout geometry. However, the Dutch railway network consists of over 6000 Switches and Crossings (S&C) (ProRail, 2021). It is logistically not feasible to measure all S&C frequently with the current fleet of measurement trains. Therefore, only turnouts that are part of the main network (defined as all remotely operable turnouts) are being monitored by geometry measurements conducted with an interval of approximately half a year.

Dedicated measurement vehicles are single-purpose, specialised vehicles that require a large initial investment. Moreover, they require a specialised crew, traction/fuel, maintenance and routes, which also makes their operation costly. To guarantee a maximum monitoring interval of half a year, redundant measurements are prescribed (requiring at least 2 passes per route). For a single regular switch this means that at least 4 occupancies are required. Therefore, this monitoring method reduces track availability significantly, albeit it being temporary. Although dedicated measurement trains give an accurate insight in the current geometry, utilisation of these vehicles only yields information with large time intervals and therefore undermines timely detection of potential problems. Moreover, their operation is costly and logistically complex.

1.1.3. In-service passenger trains as monitoring platform

ProRail aims to monitor their assets more frequently in an affordable way. Given the drawbacks and costs of utilising dedicated measurement trains, fleet expansion is not a feasible option. Therefore, simpler monitoring systems that can be installed or retrofitted on regular in-service trains are being investigated. This approach reduces upfront and operational costs, enables frequent execution of measurements and increases track coverage compared to dedicated measurement trains.

In 2021 ProRail started a tender "Reizigerstrein als Meettrein (RaM)" awarded to IBM/D-Rail to utilise in-service passenger trains as infrastructure monitoring platform. The goal was to retrofit acceleration sensors on both axle boxes of one wheelset to 14 trains of Nederlandse Spoorwegen (NS), starting with two intercity passenger trains. The ABA system is predominantly used to determine track parameters in the wavelength range of 0.5m to 10m according to the EN-13848 norm. These two intercity's have been (as part of testing and validation) in regular operation and were not fixed to a single line, thus they covered a large extend of the main Dutch railway network. ProRail was not involved in deciding where these trains ran. Therefore, from the IM's perspective, the monitoring of the infrastructure elements was random. Many individual S&C have been passed with varying time intervals. These initial in-service passenger train ABA measurements (confidential and not publicly available at the time of writing) form the basis for the proposed assessment method for the structural health of individual crossings.

1.2. Problem statement

Railway turnouts, also known as S&C, have become an essential part of modern railway networks. Fixed crossings within turnouts introduce a discontinuity in the rail to accommodate the passing of train wheel flanges. As a consequence, the crossing of a railway turnout is subjected to severe wheel-rail contact conditions and high dynamic, repetitive loading. These conditions cause wear, plastic deformation and Rolling Contact Fatigue (RCF) leading to even worse wheel-rail contact conditions. Ideally, these mechanisms are predictable and thereby maintenance can be conducted effectively. In practise however, degradation is uneven (both temporal and spatial) and hard to predict. This is mainly caused by the large amount of variables and randomness of the dynamic train-track system due to imperfections (e.g. material, geometry, support) and variation in local environment (e.g. soil conditions, weather). SHM tries to give insight in the current state of the infrastructure. However, the current strategy of monitoring turnouts is based on measurements with large time intervals, undermining effective maintenance and timely detection of potential problems.

1.3. Research objective

Timely detection and assessment of the structural health of crossings enables railway IM's to perform tailored, information-driven maintenance. This reduces maintenance costs due to substitution of costly replacements by timely low-cost corrective maintenance or preventive/predictive maintenance. This elongates the life-time of crossings, potentially lowers maintenance costs and prevents sudden failures and following disruptions. The assessment of the structural health of crossings on a regular basis and timely detection of degradation is therefore desired. Utilising Axle Box Accelerations on in-service passenger trains enables frequent execution of measurements with a large network coverage. Therefore, the objective of this research is to propose an assessment method for the structural health of crossings using in-service passenger train Axle Box Accelerations.

1.4. Research questions

The research objective can be translated into the following main research question:

> *How can in-service passenger train Axle Box Accelerations (ABA) be utilised to assess the structural health of a turnout crossing?*

To answer the main research question, the following sub-questions are addressed:

- *Q1 What are the degradation mechanisms of crossings?*
- *Q2 How should in-service passenger train ABA data be processed such that it accurately represents the crossing's structural health?*
- *Q3 What is a suitable method to identify degradation of individual crossings based on in-service passenger train ABA?*

1.5. Scope

The most common regular turnout in the Netherlands is the GW 54E1 R195 1:9 (regular turnout with UIC54E1 rails, radius 195 m, intersection angle 1:9), which is seen in Figure 1.1. It can be left or right-handed, the rails are indirectly mounted (with rail chairs) on concrete sleepers and the crossing is either cast or constructed. Only this turnout type with constructed crossing is considered in this thesis. In the past years, several suppliers have merged in to the current two suppliers: Voestalpine and Vossloh Cofiger Kloos (Vossloh). Two slightly different constructed crossings exist, which is coupled to the production method of the current two manufacturers:

- Voestalpine mills a forged steel block in to a crossing nose. Wing rails are welding and bolted with distance blocks to the crossing nose.
- Vossloh constructs crossing noses by gluing and bolting milled standard rails. The wing rails are elevated by special base plates.

The ABA measurements are collected from February 1st 2022 to December 31st 2022 by two in-service passenger trains. No distinction is made between measurements from the two in-service measurement trains. Effects due to the uncontrolled measurement conditions (e.g. vehicle orientation, vehicle loading, season, weather, etc.) are neglected. Turnouts of interest are all part of the main railway network and scattered over the Netherlands. They are in varying conditions and have varying usage and age. Only turnouts with a minimum of 45 valid (see Section 3.4.2) measurements (once a week on average) driven in the facing direction on the thought route are considered.

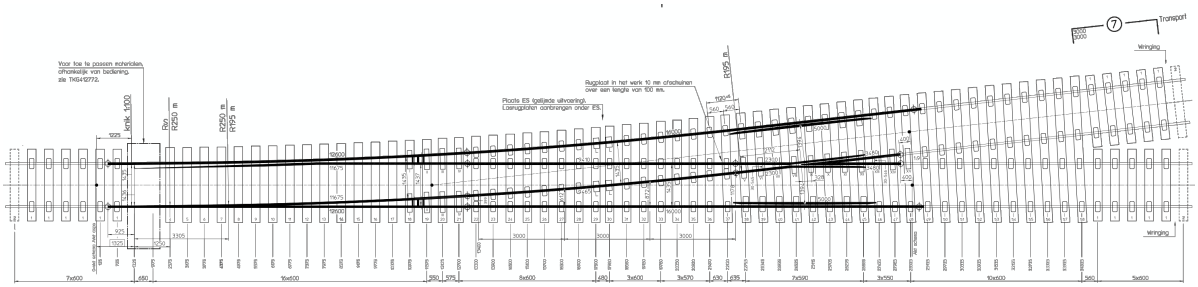

Figure 1.1: Technical drawing of the Dutch turnout GW 54E1 R195 1:9. Adapted from ProRail, 2020.

1.6. Thesis outline

In the previous sections, an introduction is given. In Chapter 2, the kinematics and dynamics of the wheel-rail contact during the passing of a crossing panel are studied. A coupling is made between the wheel-rail contact and degradation mechanisms. This lays the foundation for the monitoring setup, that is elaborated in Chapter 3. The measurements are explored and the current setup is evaluated. Chapter 4 presents the proposed assessment method and its performance for individual crossings. Conclusions and recommendations in Chapter 5 finalise this thesis.

2

Wheel-rail contact at the crossing

2.1. The crossing panel

The crossing panel is part of a railway turnout (or S&C). Turnouts enable tracks to intersect at the same level and thereby enable trains to change tracks while moving. It facilitates efficient operation by introducing flexibility of routes in a railway network. Therefore, turnouts have become an essential part of railways. A turnout can be travelled in the through or divergent route, in both facing and trailing direction. Dutch turnouts are often categorised by the intersection angle of the turnout (e.g. 1:9). The major turnout components are shown in Figure 2.1.

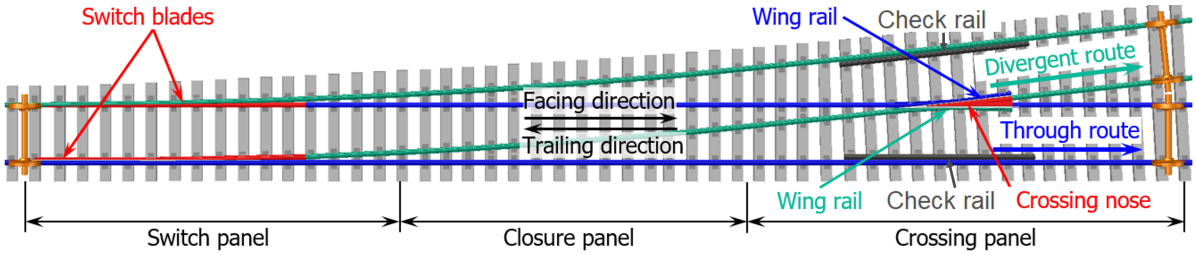

Figure 2.1: Overview of a regular left-hand railway turnout. Adapted from Liu, 2020.

Globally, a turnout can be divided in three panels. Within the switch panel the switch blades are movable and are operated via switching machines (or point machines, not shown). The state of the movable switch blades determine the route of travel. The crossing panel provides the physical intersection of two level tracks. Train wheels have a flange, as seen in Figure 2.2. Therefore intersecting rails are required to have a gap to let these flanges pass (the flangeway). This is facilitated by the wing rails and the crossing nose (or frog), together forming the intersection part of the crossing panel, called the crossing. Check rails (or guard rails) prevent wheels passing at the wrong side of the crossing nose. Lastly, the closure panel connects the switch panel and the crossing panel by closure rails.

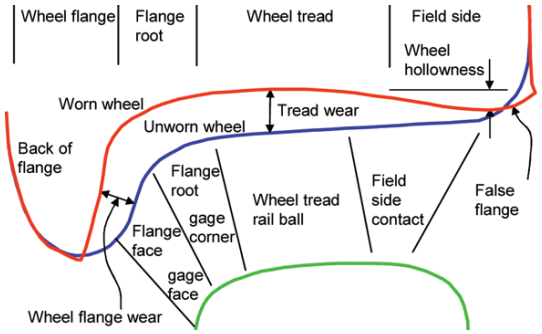

Figure 2.2: Naming of wheel and rail segments. Modified from Esveld, 2001.

2.2. Wheel-rail contact at the crossing

2.2.1. Kinematics

The design of a fixed crossing ensures flange clearance while still providing support for the wheel, while it passes the crossing. Figure 2.6a shows the flange clearance (the space between the wing rails and crossing nose). This allows some lateral displacement of the wheelset with respect to the centre of the track. If the wheelset is laterally (almost) centred, the transition is considered as regular. In Figure 2.3 the kinematics of a regular transition is visualised at specific stages for a crossing with nominal geometry. The following stages during the transition can be distinguished:

1. Regular wheel-rail contact while travelling along the switch rail.
2. The point of contact starts shifting towards the field side of the wheel due to the switch rail transitioning in to the wing rail.
3. The contact point has shifted towards the field side of the wheel. The tip of the crossing nose is located at Theoretical Point (TP). There is no contact between the wheel and the crossing nose.
4. The crossing nose levels with the wing rail. There is contact between the wheel field side and the wing rail and there is contact between the flange root and crossing nose.
5. The contact has fully transitioned to the crossing nose. The contact starts shifting from the flange root towards the wheel tread.
6. The contact shifted towards the wheel tread and can be considered as regular wheel-rail contact.

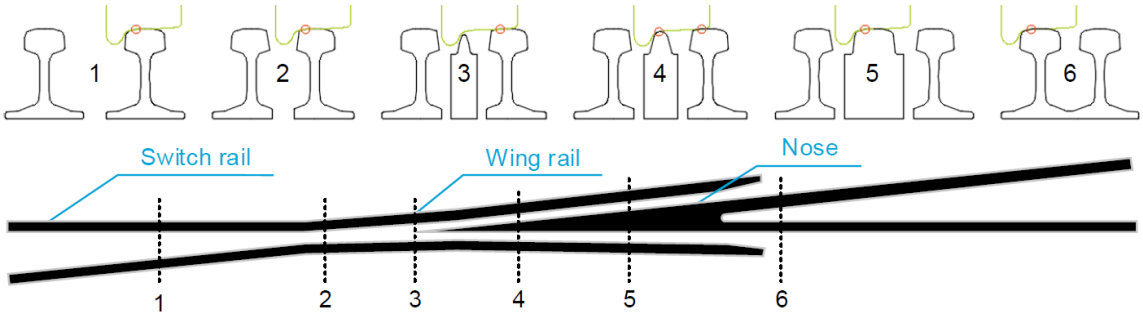

Figure 2.3: A crossing with regular wheel-rail contact stages. Adapted from Wegdam, 2018.

However, not every passing of a crossing can be considered as regular. Since trains are exited by randomness (e.g. hunting or bad track alignment) it is not known a priori what the lateral displacement of the wheelset is. To guarantee a safe passing of the crossing, the lateral displacement of the wheelset is restricted by the wing rails, crossing nose and check rails. The restricted lateral positioning of the wheelset alters the wheel kinematics and wheel-rail contact, giving rise to lateral dynamic forces.

2.2.2. Lateral dynamics

Varying the lateral displacement of the wheelset yields all possible contact situations. In this thesis, only the wheel-rail contact at the crossing side is considered. This implies that it is assumed that potential contact between wheel and check rail yield relatively low lateral accelerations with respect to the impact conditions at the crossing (as elaborated later in this section). Furthermore, the effect of the check rail on lateral positioning of the wheelset is accounted for indirectly by distinguishing regular contact and irregular contact. These contact situations are caused by restricted lateral displacement by:

- The wing rail, causing contact between the flange back and wing rail, or
- The crossing nose causing contact between the flange root and crossing nose.

The instances where the point of contact fully transitioned from the wing rail to the crossing nose are visualised in Figure 2.4. The red dots indicate points of contact between the wheel and crossing. The acceleration in the vertical direction a_y, the lateral direction a_z and the resultant a_{yz} are shown as black arrows. The angle of a_{yz} with respect to the horizontal plane is defined as α. The regular contact

situation in Figure 2.4a is taken as a reference situation, where there is no lateral displacement. In this situation there is a single point of contact which is predominantly oriented in the vertical direction, therefore the resultant acceleration vector has an impact angle $\alpha \sim 90°$.

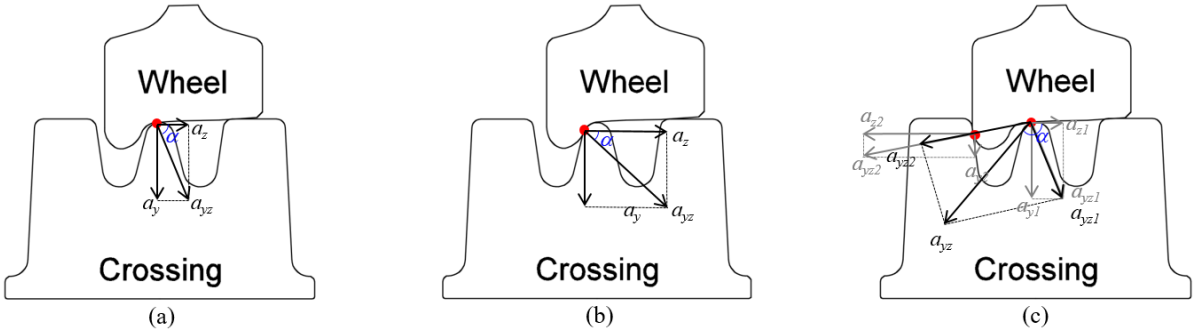

Figure 2.4: Accelerations experienced by the crossing during wheel-rail contact in facing direction. Red dots indicate points of contact. a) Regular passing; b) Flange corner-crossing nose contact; c) Flange back-wing rail contact. Adapted from Liu, 2020.

An analysis of the contact solution of rolling contact during the transition of a fixed crossing has been conducted in Wei, 2018. This study shows by means of numerical modelling that the lateral forces originating from the wheel-rail contact at the crossing have two major contributions: surface shear traction (in-plane contact force) and normal forces (out-of-plane contact force), as visualised in Figure 2.5. The study further shows that the surface shear traction is caused by lateral creep forces (frictional forces) in the wheel-rail contact interface. Moreover, the lateral contribution of the normal force is related to the contact angle, which in turn is mostly determined by the location of contact. The contribution of the contact angle to the lateral force was found to be dominant.

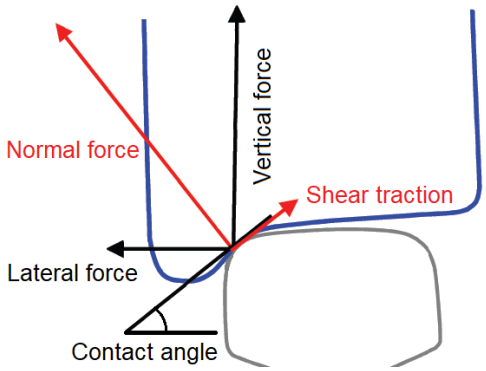

Figure 2.5: Components of wheel-rail contact forces on the wheel during flange root contact.

The effect of a large lateral contribution due to a large contact angle occurs in the irregular contact situation shown in Figure 2.4b. The wheelset has a maximum tolerated lateral displacement towards the crossing nose. There is a single point of contact, located on the side of the crossing nose and the flange root. The contact angle is large, causing the normal force to have an relative large lateral component. Therefore, this contact situation results in an high lateral dynamic force resulting in an resultant a_{yz} with $\alpha < 90°$. This is confirmed with Multi-Body System (MBS) simulations, elaborated in Appendix A.

The other extreme lateral displacement is towards the wing rail and is shown in Figure 2.4c. This irregular contact situation consists of two-point contact. The contact point located in the wheel tread is similar to regular contact. The accelerations originating from the contact point located on the flange back are predominantly oriented in the lateral direction. Moreover, in the latter contact point there is a large velocity difference between the wheel and rail leading to geometric spin (frictional torque) in the contact interface. The resultant acceleration of both contact points a_{yz} can be constructed by the superposition principle. This yields an $\alpha > 90°$.

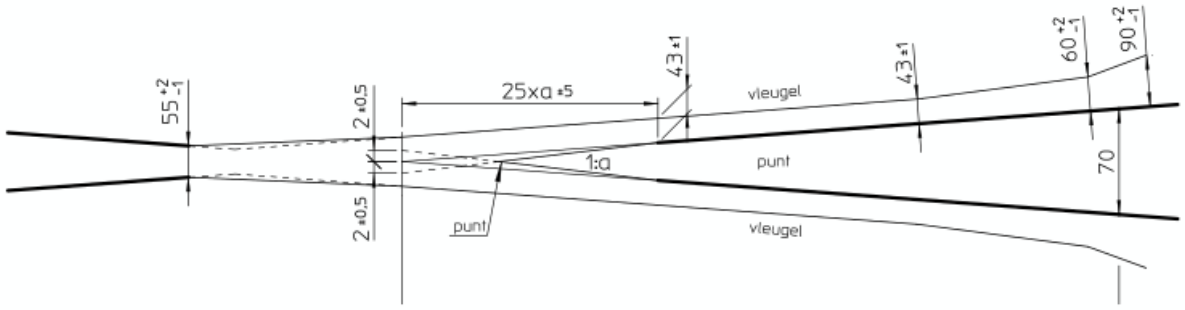

(a) Top view of a crossing with wing rails ("vleugel") and crossing nose ("punt").

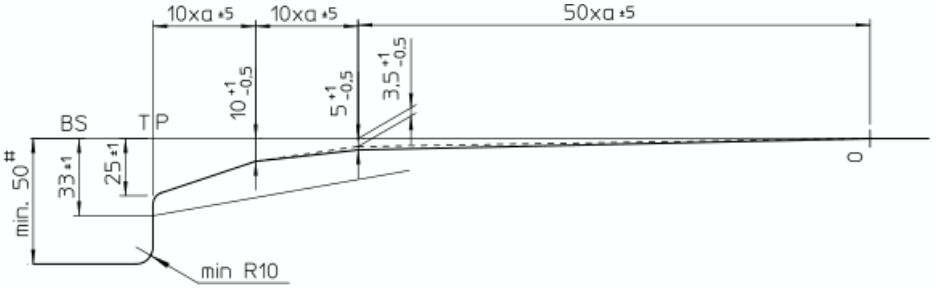

(b) Longitudinal profile of the crossing nose.

Figure 2.6: Technical drawings (aligned) of a fixed Dutch crossing panel with intersection angle α. Adapted from ProRail, 2018.

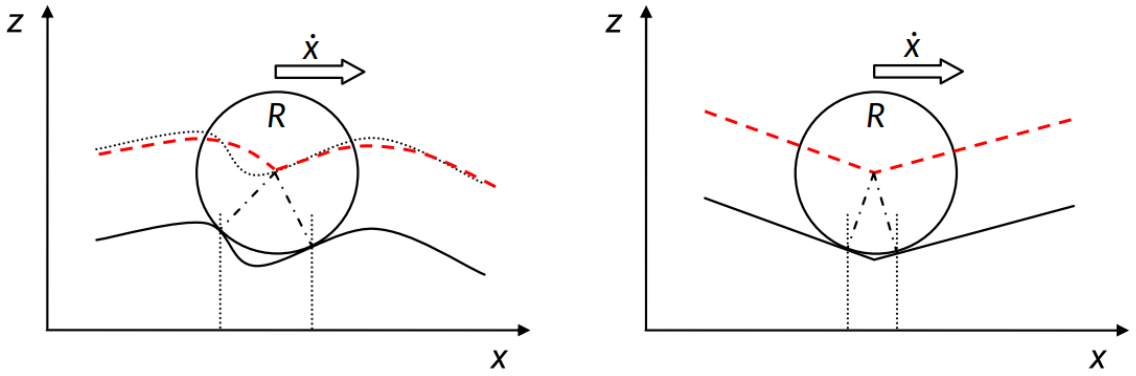

Figure 2.7: Two scenarios of 2D two-point contact causing an abrupt change in the vertical wheel trajectory (red dashed line). Modified from Steenbergen, 2008.

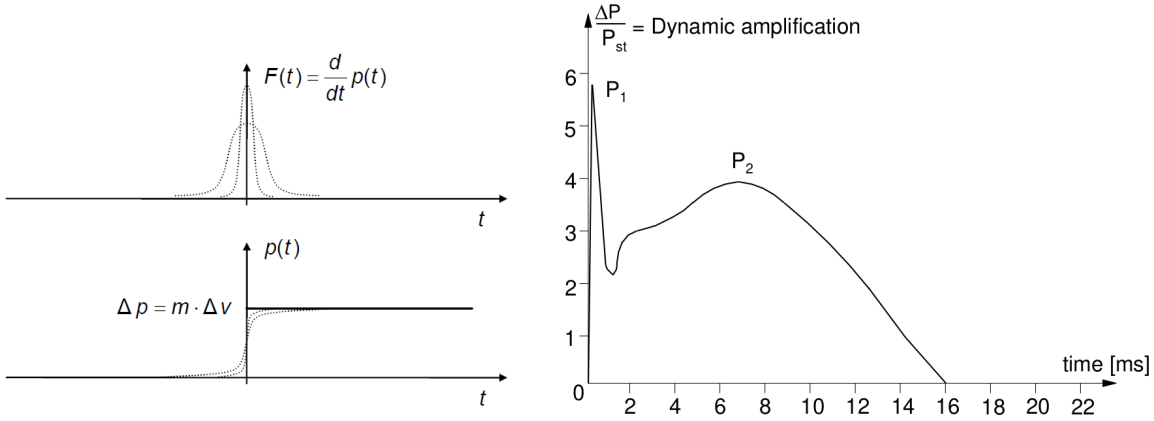

(a) An abrupt change in vertical momentum $p(t)$ causing a dynamic impact force $F(t)$. Modified from Steenbergen, 2008.

(b) Dynamic amplification due to short-wave rail irregularities (Jenkins et al., 1974). Adapted from Wan, 2016.

Figure 2.8: Vertical dynamic forces due to short-wave-irregularities.

2.2.3. Vertical dynamics

As a starting point, the vertical dynamics at a crossing are generalised to an ideal 2D case (neglecting lateral dynamics). In this case there is a round wheel with radius R that runs with a velocity of $\dot{x}$ along a straight rail without irregularities. A single point of contact exists between the wheel and rail. Since the trajectory of the wheel centre is dictated by the vertical rail geometry, the wheel trajectory is parallel to the rail. The wheel inertia does not contribute to the vertical contact force and the direction of the wheel does not change. Thus the vertical load consists only of the gravitational static load. Generally, if the wheel centre trajectory changes from being a continuous straight line, the wheel inertia gives rise to dynamic amplification of the static wheel-load. In case of a short-wave rail irregularity ($\ll R$), as seen in Figure 2.7, two-point contact arises and the trajectory of the wheel abruptly changes direction (Steenbergen, 2008).

Under the assumption of rigid bodies and pure rolling, the time-derivative of the wheel trajectory represents the vertical wheel velocity. Therefore, discontinuity in the trajectory implies a discrete change in vertical momentum. As visualised in Figure 2.8a, the change in vertical momentum Δp is proportional to the change in vertical velocity Δv. A vertical force $F(t)$ is caused by the change in vertical momentum. $F(t)$ is equal to the time derivative of $p(t)$ and therefore the amplitude of $F(t)$ has a time-dependency that translates to the horizontal wheel velocity $\dot{x}$. The more abrupt the vertical velocity changes, the higher the amplitude of $F(t)$. Therefore, an abrupt change in the wheel trajectory causes dynamic amplification of the static wheel load. The resulting impact force $F(t)$ is proportional to the change in vertical momentum Δv and the horizontal wheel velocity $\dot{x}$.

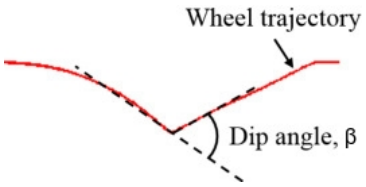

Figure 2.9: Wheel dip angle. Modified from Torstensson et al., 2019.

Jenkins et al., 1974 demonstrated with a simple dynamic model that the response to a short-wave irregularities can be characterised by two components: a high frequency (200–1000 Hz) force immediately after the impact (known as the P1 force) followed by a low frequency (50–200 Hz) peak of reduced magnitude (known as the P2 force), as seen in Figure 2.8b. These simple models hold well for e.g. welds or dipped joints since there is no significant physics involved in the lateral direction (Steenbergen, 2008). This is not the case for crossings, where the lateral dynamics are significant. However, the vertical wheel trajectory varies in a similar fashion while it travels over a fixed crossing: a downwards motion changing abruptly to an upwards motion as the contact transitions from the wing rail to the crossing nose (Wan, 2016; Wei, 2018). Moreover, complex irregular transitions (as a result of a laterally displaced wheelset) and varying crossing geometry also show vertical trajectories with this characteristic as demonstrated by the numerical simulations conducted by Wan, 2016.

The abrupt change in the vertical wheel trajectory can be modelled by the concept of a dip angle as defined in Figure 2.9. The dip angle captures the change in vertical momentum Δv, together with the horizontal wheel velocity $\dot{x}$ the wheel dip angle can be used as estimator for the vertical impact forces. It has been demonstrated experimentally and numerically (Johansson et al., 2011; Liu, 2020; Wei et al., 2017) that crossing geometry degradation cause an increase of vertical impact forces. High impact forces caused by degradation should therefore coincide with large wheel dip angles. Therefore, large wheel dip angles can function as an estimator for degraded crossing geometry.

The mentioned studies have not reported dip angles among their findings. However, the reports show (indirect) evidence for this relation between dip angles, impact forces and degradation. In Liu, 2020, acceleration measurements of one crossing nose at three different states of degradation are reported. The maximum vertical crossing acceleration is significantly higher (50-100%) for a degraded crossing. The increased acceleration amplitudes indicate an increase in impact forces and therefore also an increased dip angle. In the same study it is also shown that in case of a damaged crossing the longitudinal wheel impact locations become more localised. More localised impact locations imply a shorter transition region which also suggests increased dip angles. This further hints that dip angles have increased with more severe crossing degradation (Torstensson et al., 2019). Although not explic-

itly stated, Wan, 2016 is in agreement by demonstrating within a numeric modelling parameter study that by varying the longitudinal profile of the crossing nose unfavourably, both the wheel dip angles and impact forces increased.

2.3. Degradation of crossings

The jump in contact at the transition from wing rail to crossing nose cause high impact forces. The repeating impacts causing high stresses are a source of degradation: plastic deformation. Over time, plastic deformation accumulates due the cyclic impact loading (ratchetting). Cracks can develop and once there are cracks, they propagate. This process is called Rolling Contact Fatigue (RCF). Some examples of plastic deformation and RCF can be seen in Figure 2.11. Crossings commonly suffer from both plastic deformation and RCF (Wan, 2016).

The second type of degradation is wear which is caused by relative velocity differences between the wheel and rail, e.g. during flange back contact as elaborated in Section 2.2.2. Adhesion and sliding in the wheel-rail contact cause material removal whereby severe deviating rail and wheel profiles arise. These profiles result in undesired dynamical effects, ranging from slightly reduced ride comfort to full loss of contact and possibly derailment (Wan, 2016). Commonly, large velocity differences exist during flange-rail contact. This causes large frictional forces and excessive wear. Besides undesired dynamic effects, wear can also contribute to catastrophic wing rail breakages (Shevtsov, 2023) as seen in Figure 2.10.

(a) Broken wing rail at Oudewater, turnout 93A (2017) with visible wear on the wing rail.

(b) Broken wing rail at Gouda Goverwelle, turnout 465B (2018).

(c) Wear on the wing rail of turnout 465B (2018).

Figure 2.10: Two severe rail breakages in crossing panels with significant wear on the wing rails. Adapted from Shevtsov, 2023

Degraded track and turnout geometry amplifies dynamic forces. The P1 force's high frequency characteristics cause the force to be present very briefly, whereas the P2 for lower frequency causes the P2 force to be present relatively long. As a consequence, localised degradation arises from P1 forces whereas P2 forces cause degradation to components in the surroundings of the impact area such as fastening system, rail pads, sleepers and the ballast bed. In turn, the degraded crossing geometry amplifies dynamic forces, leading to more track deterioration. Degradation mechanisms have an accelerating character and degradation of the crossing geometry can be considered as the source of many other degradation mechanisms. By reducing degradation of the crossing (e.g. by timely maintenance), both the high-frequency P1 forces and lower frequency P2 forces will be reduced, taking away the source of many degradation mechanisms.

(a) Cracks (b) Squats on crossing nose

(c) Squats on wing rail (d) Shelling

(e) Missing bolt (f) Indention of baseplate into sleeper

Figure 2.11: Several defects in crossing panels. Adapted from Wei, 2018.

2.4. Conclusion

The crossing panel is the part where the intersection of two tracks takes place in a turnout. The wing rails and a crossing nose together form the crossing. Together, they provide the physical intersection of two rails. The wheel-rail contact transitions where the crossing nose and wing rail level. This discontinuity disturbs the wheel motion and thereby it forms an excitation in the train-track interaction at the crossings. The wheel experiences a downward motion that abruptly changes to an upward motion. This abrupt change can be modelled by the wheel dip angle, which can serve as a geometry degradation estimator. Given the steel-on-steel contact and unsprung masses of the wheel and rail, the wheel-rail regular or irregular contact transition generates high dynamic forces. In general, high impact forces are the leading causes of defects, wear, and failure of other railway components and should therefore be kept to a minimum. Plastic deformation and/or RCF is linked to the magnitude of impact forces. Wear is mainly dominated by relative velocities between wheel and rail, which is most often during flange-rail contact (irregular contact). Therefore, low vertical impact forces and preventing lateral impacts by ensuring good geometry could increase service life of crossings and other components.

At this point an answer can be formulated to research sub-question 1:
"What are the degradation mechanisms of crossings?"

> The crossing is subjected to severe wheel-rail contact due to the transition of contact from wing rail to the crossing nose. Two types of contact can be distinguished: regular and irregular. Regular contact implies a single point of contact with dynamic forces predominantly in the vertical direction. Irregular contact can be single-point or two-point contact with a large lateral component. As a consequence, three degradation mechanisms develop: plastic deformation, RCF and wear. The former two have a relation to impact amplitudes and repetitive loading, the latter with relative velocity differences between wheel and rail which is most severe during irregular transitions.

3

Monitoring

3.1. Structural Health Monitoring

3.1.1. Addressing uncertainties during service-life

Uncertainties play a large role in Civil and Structural Engineering (e.g. true loading, true material properties, environmental influences). Many codes prescribe rules to minimise risks and therefore try to guarantee a certain level of predictability and thus safety. Short and long-term effects are often captured by applying educated margins to characteristic values, turning them in to design values. However, rules and models are a simplification of reality. Not every effect is known, models do not accurately describe reality or reality is underestimated. This causes that not all effects are captured in designs. Predictions may start deviating from reality during service life, (re-)introducing uncertainties and undermining safety.

To address these potentially arise uncertainties, SHM was introduced in the 1990s as an operational variant of non-destructive testing (Viechtbauer et al., 2013). However, where (non-)destructive testing is active (excite structures to capture their response), SHM is passive. This means that under normal operational conditions the response of the structure is captured. The main advantages are the lack of needed (controlled) excitation and no reduction of the structure's availability. This is especially relevant for the Dutch Railway network given that the demand for availability is high and the network capacity is almost fully utilised.

3.1.2. Development of railway infrastructure monitoring

In recent years, railways have experienced significant increase in axle loads and operational speeds. The increased physical loading and loading rate accelerated deterioration of railway track. The made assumptions and models currently used for design of railway components are not always adapted to these recent developments. One of the effects is that lifetime expectancy's of railway components start to deviate significantly from practice. Combined with higher track utilisation and ever increasing demand, maintenance became a more prominent topic within the railway industry to guarantee safety.

However, the railway industry is known to be a conservative industry. This is backed by human visual inspection to still be a widely used monitoring system for turnouts. With visual inspection, technicians identify degradation and/or damage by either foot patrol or watching videos made by video inspection trains. This way of monitoring is labour-intensive and not very efficient. Besides, not all damages or degradation can be visually detected (e.g. sub-surface defects or hanging sleepers). Moreover, the human factor makes the judgement subjective and potentially erroneous. Due to the low inspection frequency and lack of sophisticated analysis the monitoring of turnouts is not optimal. As a consequence, turnout components barely receive maintenance and are replaced instead once they fail abruptly or are found to be heavily degraded.

3.1.3. Information driven maintenance

Although different definitions of maintenance strategies exist, they all can be classified as proactive or reactive (Gackowiec, 2019). Maintenance in the railway industry is still mainly performed reactive, in the form of repairs in case of a (severe) defect. A modern approach is to conduct maintenance before there is a (disruptive) defect: proactive maintenance. The main benefits of this approach are minimisation of unforeseen disruptions (higher track availability), lower maintenance costs (performing low cost preventive maintenance actions instead of costly replacements) and the ability to plan and prioritise maintenance in advance (optimal use of limited maintenance capacity). This approach requires reliable information of the current state of the track, and of knowledge of deterioration mechanisms to predict failure of the track components with respect to time. However, more often than not the current track state is unknown or uncertain and therefore SHM is desirable for railway IM's.

One can distinguish two major forms of railway SHM systems: wayside or vehicle-based. Wayside systems are static measurements systems capturing temporal signals. They are installed on, or close to, track components. Vehicle-based systems are mounted on rolling stock, and are therefore dynamic monitoring systems. These signals do not only have a temporal but also a spatial component. SHM methods most often cannot directly measure damages. Therefore, physical properties of a structure (response) are measured, e.g. eddy current, image-based or accelerations. From this measurement data, damage or degradation features are extracted. A damage or degradation feature is a (derived) characteristic in the measurement data that is sensitive to the effect of damage or degradation on the structure (response), e.g. an exceptionally large acceleration amplitude can imply impact forcing that potentially damages the structure.

Depending on the available information/sensors and analysis, SHM methods and systems can be categorised into four levels (Rytter, 1993):

1. Detection (qualitative indication that there might be damage)
2. Localisation (information about the location of the damage)
3. Assessment (information on the size of the damage)
4. Consequence (actual change in structural behaviour or safety due to damage)

Level 1 is a basic form of monitoring by anomaly detection. Either a comparison against a groundthruth measurement is made or educated thresholds are set. Level 2 also has a spatial component, often this is simply capturing the location of the sensor in the time domain. Level 3 involves analysis of the detection and location and estimates or predicts the severity of the detection. This requires knowledge about the physics involved and characteristics of the structure. Lastly, level 4 not only estimates the severity, but also analyses the effect on the structure's behaviour (impact on safety). This often requires a sophisticated and calibrated physics model of the structure, nowadays called a 'Digital Twin'. For railway infrastructure, a SHM system of level 1 will be the equivalent of searching for a needle in a haystack, therefore level 2 is the minimum feasible level. However, level 3 enables efficient maintenance strategies by prioritising based on severity which is desirable for railway infrastructure.

3.2. Crossing monitoring

3.2.1. Purpose

The geometric discontinuity between the wing rail and crossing nose induces dynamic wheel-rail contact forces, as elaborated in Chapter 2. These forces cause degradation of the crossing in the form of RCF, wear and/or plastic deformation. This is true for nominal geometry, however the dynamic wheel-rail interaction worsens on degraded crossing panels, which increases contact forces resulting in accelerating degradation mechanisms. To break the accelerating degradation loop, manual maintenance actions are carried out by technicians, e.g. grinding and welding. This causes variety in the quality and precision of maintenance. The conducted maintenance may not always be satisfactory or even beneficial. Other components, e.g. rail pads, sleepers and ballast, also suffer from high wheel-rail contact forces and deteriorate. This increases the risk of unforeseen failure and causes danger to safe train operation. Consequently, turnouts contribute to a large portion of the maintenance or renewal costs of railway infrastructure. E.g. Pålsson and Nielsen, 2012 report a contribution of 13% of the total yearly maintenance costs in Sweden in 2012. If the IM does not identify degradation and plans maintenance accordingly, life cycle costs will rise and failures become a significant risk. Therefore it is desired to monitor the structural health of a crossing.

3.2.2. Vibration-based monitoring

The limitations of visual human inspection lead to the development of monitoring technologies that are based on physical principles. The train-track system is a dynamic system, inducing dynamic forces. Accelerations and dynamic forces are related to each other, therefore monitoring based on vibrations is a rational approach. Both wayside systems (e.g. Liu, 2020) and vehicle-mounted systems (e.g. Li et al., 2015) have been found applicable.

In this thesis, a vibration-based, vehicle-mount system is utilised by measuring Axle Box Accelerations (ABA). The axle box is the closest location to the wheel-rail interface that is stationary. Therefore it is simple to mount a sensor and the accelerations resemble the wheel-rail forces. Earlier research shows that ABA is capable of detecting both isolated defects (e.g. squats (Molodova et al., 2014), degraded insulated joints (Molodova et al., 2016)) and periodic defects (e.g. rail corrugation (Massel, 1999)). Liu, 2020; Wei et al., 2017 have shown that vibration-based methods are suitable as monitoring system for crossing noses, either by wayside as by vehicle-based systems. The advantages of ABA compared to other systems are the lower cost, ease of installation and maintenance, ability to operate at operational speeds and possibility to retrofit existing vehicles (Li et al., 2015).

The assessment methods proposed in earlier studies (e.g. Molodova et al., 2014, Molodova et al., 2016, Li et al., 2015, Wei et al., 2017) are all based on time-frequency analysis with the aim of identifying dominant frequency bands (resonances) that have a large contrast in energy levels between a nominal and degraded state. The identification of relevant frequency bands requires sufficiently high sampling frequency to prevent aliasing. The prior mentioned studies therefore measured all with a sampling rate close to 25.6 kHz. To cope with random errors and effects during measurements (e.g. due to hunting), multiple measurements are aligned and combined into a single signal that is further analysed. This requires a controlled environment, i.e. controlled measurement vehicle operation. It is only meaningful to combine signals into a single signal that have been conducted under similar conditions (e.g. same vehicle, location, speed). This is why often a dedicated measurement vehicle like Centrum Technologisch Onderzoek (CTO) is used. This is fundamentally different to mounting sensors to passenger trains, which basically make the measurement environment highly uncontrolled.

3.2.3. In-service passenger trains as monitoring platform

In 2018, ProRail started the project ”Camino” in collaboration with NS. One of the goals of this project was to create a proof of concept of monitoring railway infrastructure from in-service passenger trains. The reasoning behind starting this project is the large interval in between measurements from dedicated track geometry measurement trains. The idea was that in-service passenger trains could detect degradation or defects timely, laying the basis for short interval monitoring and information-driven maintenance. The proof of concept was successful, after which RaM followed in the form of a tender. The aim was to take the lessons learned from Camino and let the market come up with a robust measurement setup.

The goal of the RaM project is to mount the monitoring system to 14 in-service passenger trains (three different types) and to measure track geometry parameters according to EN-13848. In addition, exploiting the measurement data for detection and monitoring of local defects potentially lays the basis for short interval monitoring and data-driven maintenance. Besides developing and installing monitoring hardware was basic processing also part of the tender. In the form of a dashboard measurements would be displayed, accompanied by automatically detected anomalies (”alarms”) if impact or track geometry thresholds would be exceeded. This tender setup caused that all processing and development is done by the winning market party. From an IM perspective, this could be beneficial since the system installation, operation and verification is all conducted by the supplier. The downside however is that the inner workings and processing algorithms are not fully transparent, obfuscating what the output consists of and represents. It also puts trust in the market party having knowledge of measuring, sensors, signal processing, IT-infrastructure and train-track dynamics. It is not common to have expertise in all these areas.

3.3. Measurement setup

3.3.1. Hardware specifications

In Figure 3.1 the measurement setup is shown. This solution is a commercially available system from the company D-Rail AB. Two sensors are mounted, each on an axle box of a single wheelset on a trailing bogie. The sensors are 3D capacitive Microelectromechanical System (MEMS) accelerometers. Capacitive MEMS accelerometers are based upon electrical capacitance changes that are induced by a (microscopic) seismic mass under acceleration. The sensors are powered and connected via a serial cable to a Peripheral Wireless Measurement Device (PWMD) that is responsible for collection and chronically storing measurement data generated by the sensors. It is mounted in the bogie and runs on a battery. The PWMD transfers the measurement data to the Main Processing Unit (MPU) wirelessly. The MPU is mounted in the car body and powered by the on-board power supply of the train. After aggregation with GPS positioning data, the MPU sends the measurement data via the cellular network (4G) via secure VPN to a land-side server.

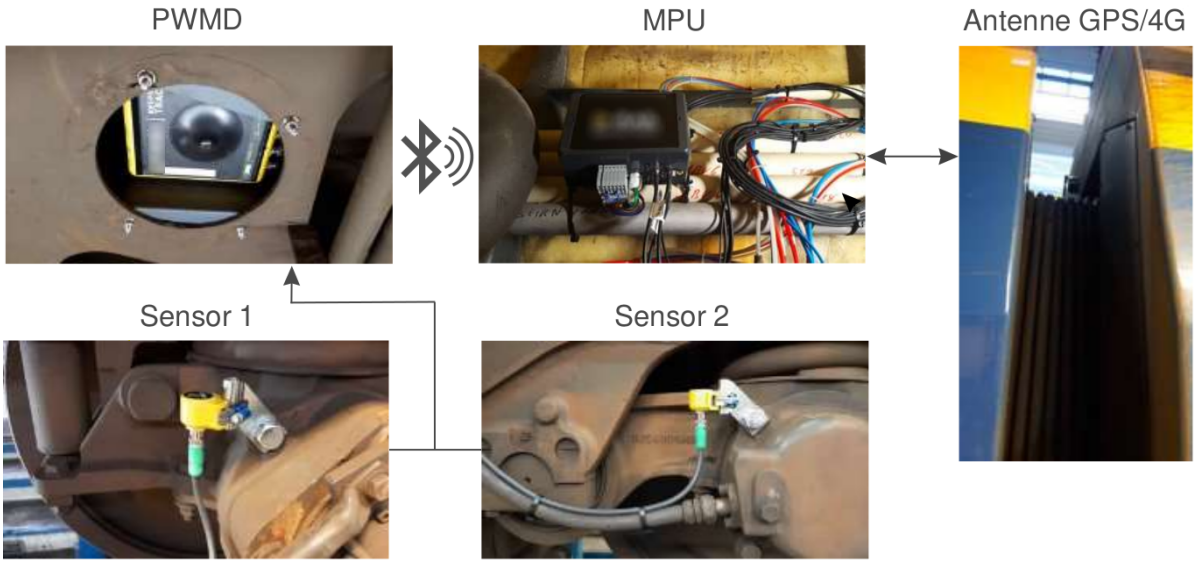

Figure 3.1: Components of the ABA measurement setup of RaM. Modified from Kruse, 2022.

Acceleration is a physical, continuous (analog) signal. To capture this signal, an accelerometer (acceleration sensor) is used which transforms an analog acceleration signal into an analog electrical signal. Effectively it maps acceleration amplitude to electrical quantities (e.g. voltage, current). But this is never a perfect mapping, therefore different sensor designs exist that are optimised for different characteristics (e.g. large input range, precision). Moreover, an Analog to Digital Converter (ADC) is used to sample (capture the analog sensor signal at an instance), creating a digital (discrete) representation of the analog signal. This is required to be able to process signals with digital computers.

The sensor and ADC design dictate the accelerometer characteristics. Some designs allow user selected settings, altering the characteristics. Full Scale (FS) defines the range of physical acceleration amplitude that can be accurately captured by the sensor. The resolution is the amount of discrete values (bits) the analog signal is discretised into by the ADC (e.g. 16 bits equals 65536 values). The Least Significant Bit (LSB) follows from the resolution, which is defined as the lowest bit in binary which corresponds to the smallest factor a signal can be divided into (e.g. for 16 bits, the LSB equals 1/65536). The sensor sensitivity is the minimum amplitude that can be output, determined by the FS range divided by the resolution. Mechanical systems are influenced by temperature, altering its properties. Therefore the sensitivity of the sensor changes due to temperature differences, which is specified as the temperature sensitivity. The zero-g level offset accuracy is the amount of measured acceleration if there is no mechanical excitation. Sampling Frequency (SF) indicates at what frequency the ADC samples the analog signal. As elaborated in the following sections, signals are subjected to multiple sequential filters (i.e. filtering chain) that alter the signal characteristics. The Output Data Rate (ODR) is the sampling rate of the final output after the filtering chain. Bandwidth (BW) is the frequency range in which the sensor operates, defined from DC (0 Hz) to an upper limit (called the cut-off frequency). The maximum bandwidth is bounded by the mechanical resonance frequency of the sensor. However, typically the BW is DC to ODR/2, in combination with a low-pass filter with a cut-off frequency set at the upper BW bound to prevent aliasing (see Section 3.3.2). This ensures that the output signal accurately represents the measured motion for the given SF. No sensor and electrical circuit is perfect, the spectral noise density is the measured noise (non-zero measured values due to sensor and circuitry imperfections).

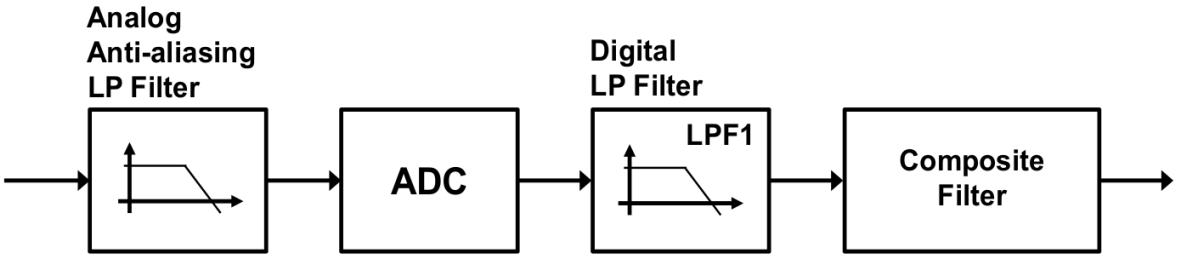

Figure 3.2: Typical processing chain for MEMS accelerometers.

A typical filtering chain is visualised in Figure 3.2, it consists of four sequential stages: an analog anti-aliasing low-pass filter, an ADC, a digital low-pass filter and a composite group of digital filters. In the current configuration, the sensor signal is passed through an analog low-pass filter prior to discretisation by the ADC. The ADC samples the signal 7 kHz. The sampled signal is then passed through an digital low-pass filter with a cut-off frequency of 52 Hz. Lastly, the composite filter has an internal First-in-First-Out module that block averages the signal over 64 data points. The output of the filtering chain therefore has a SF of 104 Hz, with a BW of 52 Hz.

3.3.2. Evaluation and verification

Sampling is the process of capturing a continuous signal (e.g. in space or time) by a sequence of discrete values. The bridge between the continuous time domain and discrete time domain is served by the Sampling Theorem. The theorem states (Shannon, 1949):

> If a function x(t) contains no frequencies higher than B Hertz, then it can be completely determined from its ordinates at a sequence of points spaced less than $1/(2\mathrm{B})$ seconds apart.

In other words: a sufficiently high sampling rate is considered anything higher than 2B samples per second. Or for a given sampling rate f_s, perfect signal reconstruction is guaranteed possible for frequencies up to $f_s/2$ (known as the Nyquist frequency). For the current measurement setup this means frequencies up to 52 Hz can be reconstructed.

As elaborated in Chapter 2, short-wave irregularities in the wheel-rail contact causes high-frequency impact forces P1, accompanied by lower frequency P2 forces. Therefore, to accurately capture the dynamics due to impact, the sampling rate requires to be sufficiently high. Previous studies (e.g. Li et al., 2015; Molodova et al., 2016; Wei et al., 2017) utilise time-frequency analysis and show that the impact

forces originating from short-wave irregularities have frequency components reaching up to 2500 Hz. For crossings frequencies up to 650 Hz have been found dominant (Wei, 2018). This means that the current measurement does not satisfy the sampling criterion. Thereby, the current measurement setup, which is primarily intended to measure track geometry parameters, does not accurately capture the wheel-rail dynamics accurately and time-frequency analysis is not applicable. Planned further releases of the sensor system potentially overcome this problem.

The filtering chain of RaM is using an so-called oversampling (much higher SF than the Nyquist frequency) and decimating (downsampling) approach. This is not uncommon in signal processing, generally it improves the Signal to Noise Ratio (SNR) by suppressing noise due to averaging. It works well if the noise is uniformly distributed among all frequencies (white noise). However, the 'noise' is not always distributed as such, therefore this approach is not suitable for every application.

To quantify the measurement setup and filtering chain, the RaM signals are "reconstructed" based on high-frequency measurements of the same turnout performed by another vehicle. On a measurement run on May 13th 2022, two turnouts within the scope of this thesis were measured by CTO, TU Delft's own measurement vehicle. RaM also passed these turnouts at least once a week in May 2022. The vertical accelerations of the last trailing axle from CTO is used as reference, after low-pass filtering and downsampling to 6400 Hz. This corresponds more or less to a sampled signal after the ADC stage from RaM. The results is seen in Figure 3.3, together with the measurements from RaM. The signature of both measurement systems are similar however the impact amplitude and frequency content clearly differ. This emphasises the need for high SF data.

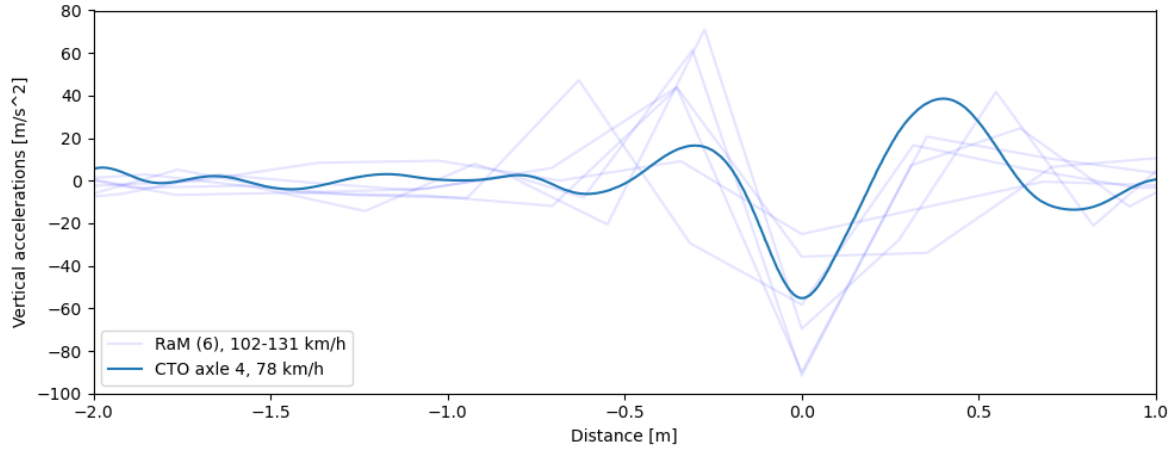

(a) Vertical accelerations on the crossing of turnout 11702026.

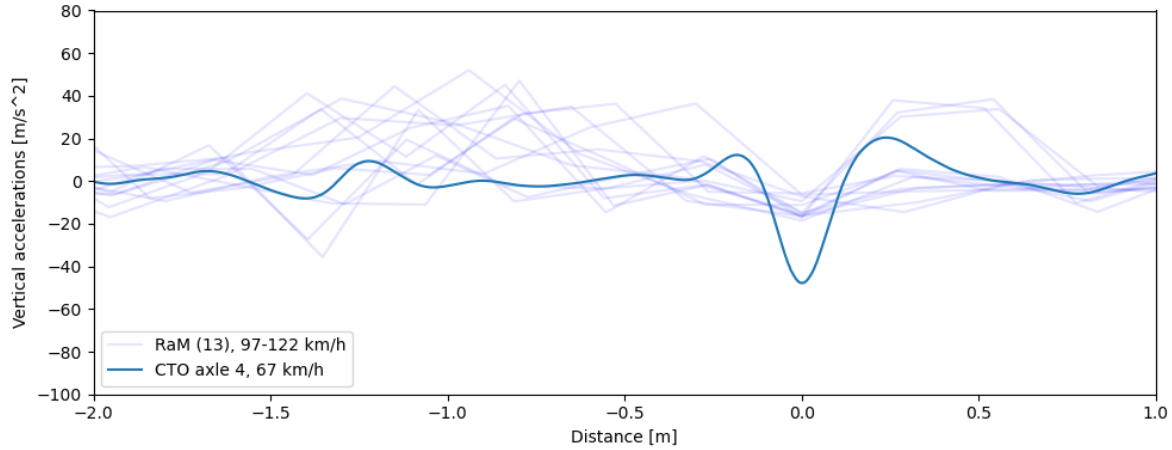

(b) Vertical accelerations on the crossing of turnout 10519266.

Figure 3.3: Vertical accelerations measurements conducted at two turnouts by both RaM and the CTO. The CTO measurement is low-pass filtered and sub-sampled to 6400 Hz.

To quantify the accuracy of the measurement setup, the RaM measurements are verified by a reconstruction based on high-frequency ABA measurements of the same turnout. The filtering chain of RaM is mimicked by applying the following stages to the CTO signal:

1. 4^{th} order Butterworth low-pass filter with a cut-off frequency at 6400 Hz as anti-aliasing filter
2. Downsampling to 6400 Hz, by decimation with a factor 4.
3. 4^{th} order Butterworth low-pass filter with a cut-off frequency at 52 Hz as anti-aliasing filter.
4. Downsampling by fixed block averaging with a block size of 64 data points.

Stage 1 is required to alter the frequency contents as anti-aliasing filter, prior to the first downsampling stage. Stage 2 downsamples the CTO measurement to 6400 Hz, which is comparable to the RaM signal after discretisation by the ADC (6664 Hz). At this point, both signals contain (almost) the same frequency components at (almost) the same sampling rate. Next, the measurement is low-pass filtered with a fifth-order Butterworth filter with a cut-off frequency at 52 Hz, similarly to the digital low-pass filter stage of RaM. This ensures that the final signal frequency components are similar for both measurement systems. Lastly, block averaging (averaging blocks of sequential data points) is used for downsampling. Three different block sizes (32, 64 and 128 data points per block) are visualised in Figure 3.4, where the block size of 64 is the same size as used in the filtering chain of RaM.

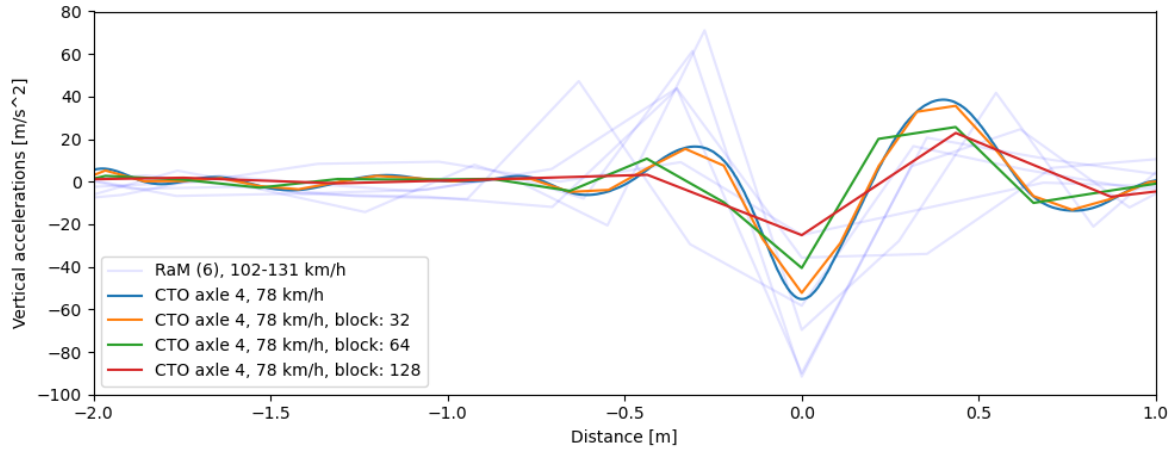

(a) Vertical accelerations on the crossing of turnout 11702026.

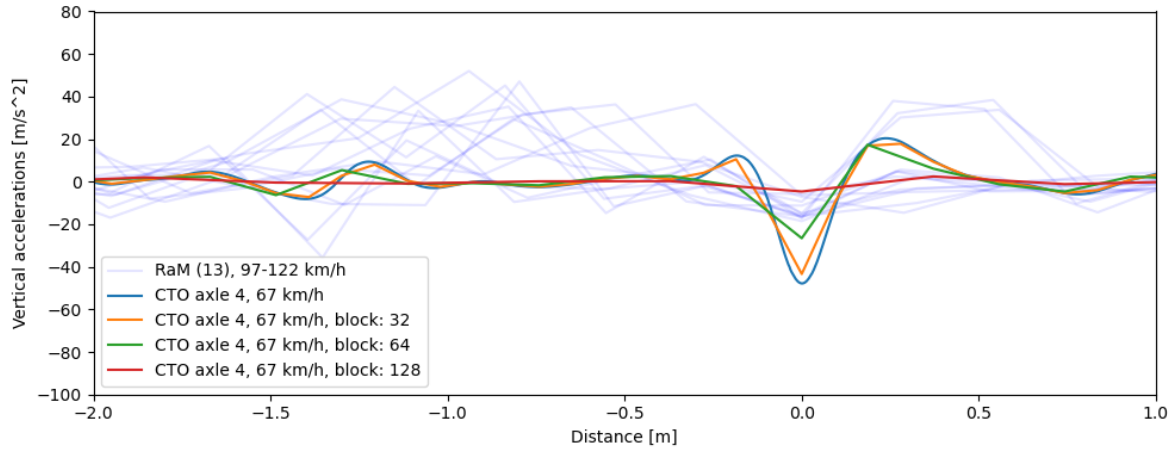

(b) Vertical accelerations on the crossing of turnout 10519266.

Figure 3.4: Vertical accelerations measurements conducted at two turnouts by both RaM and the CTO. Measurements from CTO are subjected to varying block size averaging. A block size of 64 samples coincides with the RaM filtering chain.

Downsampling can be done in varying ways of which decimation (saving every n-th sample, discard the rest) and averaging (average multiple samples in to a single value) are the most basic methods. A major difference between averaging and decimation is that decimation allocates a single data point to a larger portion in the time domain, preserving its original value, whereas averaging creates a value that is artificial. Averaging is a common signal processing technique that is used to reduce noise, especially in combination with oversampling this can be beneficial for the SNR and resolution. However, this holds for periodic signals (like heartbeat rate monitoring) where the noise is considered to be white noise (energy uniform distributed over all frequencies). Non-periodic signals with single localised peaks that are of interest (e.g. impacts) are influenced by this processing approach, which results in a low-pass filter. This effect is demonstrated in Figure 3.4 where larger block sizes reduce noise and thereby scramble the impact more.

The block averaged CTO signal shows the same signature as RaM. Clearly, the large the block size, the more it flattens the impact. The CTO signal is measured at a significant lower speed, which partially explains the lower impact amplitude. But the large spread in impact amplitudes of RaM on turnout 11702026 is remarkable. It ranges from -20 to -90 m/s^2 without a large spread in speed. Besides a possible physical explanation, there is a undesired side effect introduced by block averaging. The averaging block centre can align with an impact, not at all or somewhere in between. The alignment is random but heavily influences the averaging result. As a consequence, two hypothetically exactly similar measurements can report different accelerations and impact amplitudes by pure chance.

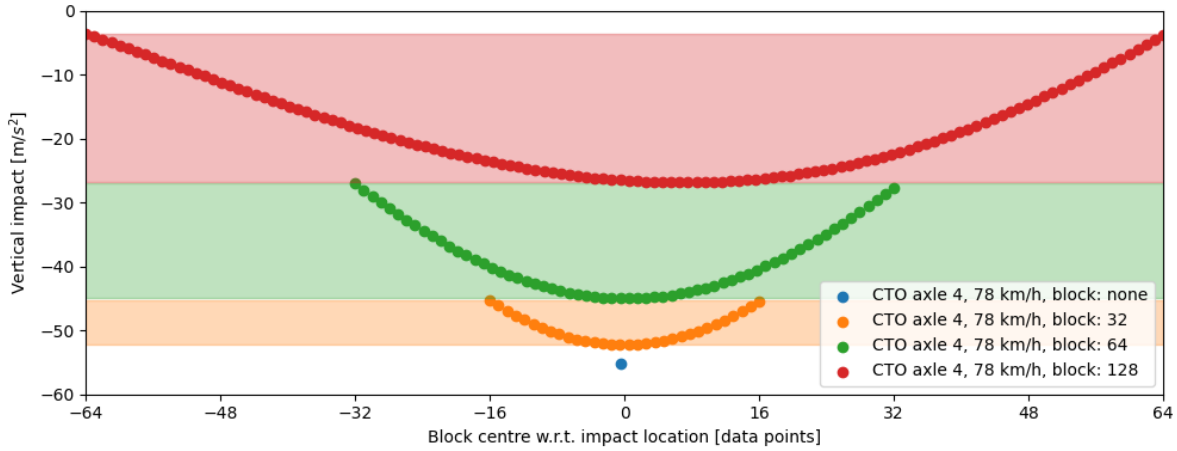

(a) Turnout 11702026.

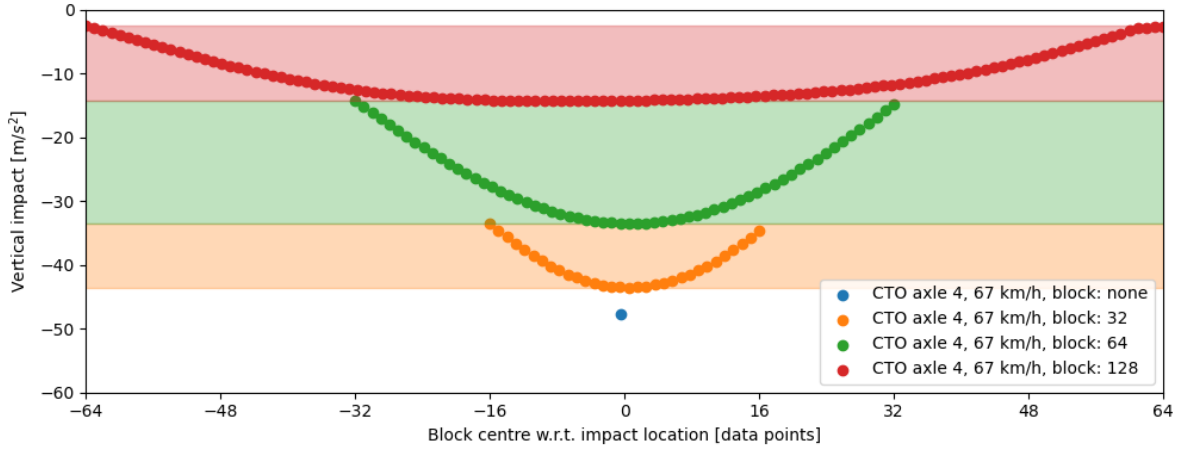

(b) Turnout 10519266.

Figure 3.5: Maximum vertical impact for varying block averaging sizes and alignment. Each dot represents the impact value for the block centre. The coloured shadows indicate the total range of impact values per block size.

This effect is demonstrated in Figure 3.5. The averaging block centre is varied with respect to the impact of the CTO measurements seen in Figure 3.3. The impact amplitude as result of averaging with specific block alignment with respect to the impact location is plotted. The true impact without averaging is the reference point. The following observations are made:

- The smaller the averaging window, the better the averaged impact amplitude represents the true impact amplitude. This is expected since a small averaging window represents the original signal better.
- The spread tends to increase with increasing block size, however this is not consistent.

For the block size utilised in RaM (64), the following observations are made:

- The absolute spread for the impact amplitude $\approx$ 20 m/s^2.
- The absolute error w.r.t. the non-averaged impact ranges from 10 to 35 m/s^2.
- The relative error w.r.t. the non-averaged impact ranges from 20 to 70%.

To demonstrate the significantly differing signals, two extreme cases of averaging block alignment are shown in Figure 3.6. This clearly shows that besides the too low SF, the measurements are also not repeatable given the introduced dependency on block averaging alignment. It must be noted however that there is a significant travelling speed difference between the CTO and RaM measurements. This causes different spatial sampling lengths, and different wheel-rail impact response.

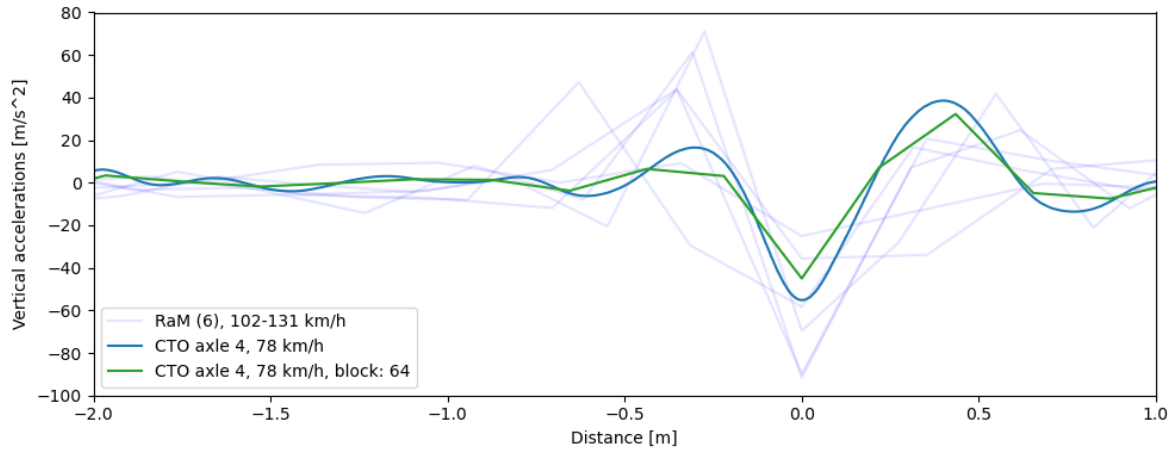

(a) Signal with the best possible averaging block alignment.

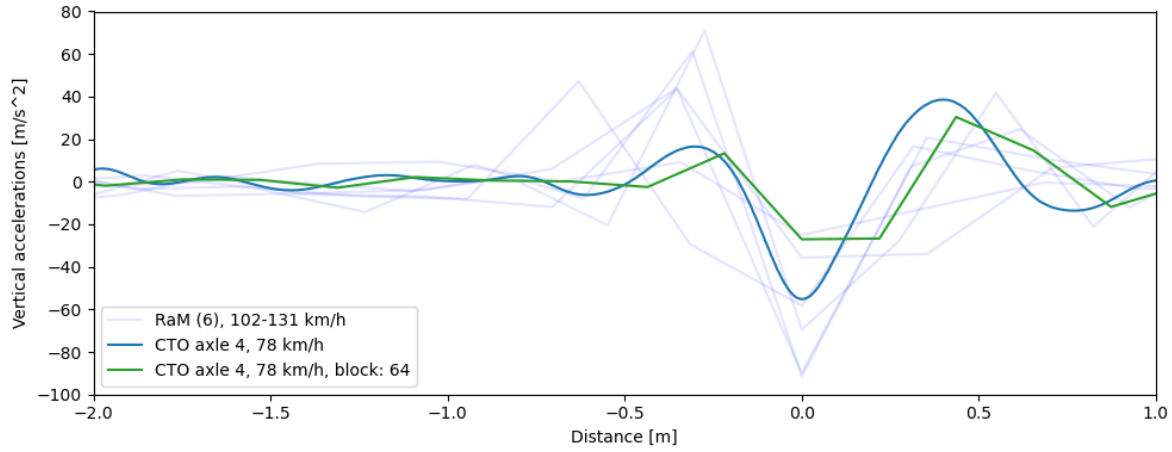

(b) Signal with the worst possible averaging block alignment.

Figure 3.6: Two extreme signals due to block averaging alignment for turnout 11702026.

3.4. Measurement processing

3.4.1. Data accuracy

As described in Section 3.3.2, the conducted measurements fundamentally lack information to accurately describe the involved dynamics. Trailing previous literature and conducting time-frequency analysis of individual signals will not yield relevant insight. Therefore, another approach is taken to still be able to assess the condition of crossings, without the ability to accurately measure the involved dynamics. The strongest feature of this measurement setup is the amount of measurements it is able to conduct (in absolute sense) and (relatively) short measurement intervals with respect to degradation speed. These features are leveraged by taking a statistical approach. Two concepts are borrowed from probability theory and statistics ("Central Limit Theorem", 2008; "Law of Large Numbers", 2008):

1. Law of Large Numbers
2. Central Limit Theorem

The Law of Large Numbers stipulates that:

> The mean of a sum of **independent** and **identically distributed** random variables converges toward the **expected value** of their distribution when the **sample size tends toward infinity**.

Individual measurements (**samples**) are a separate passing and therefore the measurements are **independent** from each other. Assuming gradual degradation of crossings, leveraging the short measurement intervals of the measurements and accounting for important train conditions (i.e. speed) implies that measurements are taken under similar crossing conditions. Therefore they can be considered **identically distributed**. This satisfies the requirements of the Law of Large Numbers and thereby the set of measurements converge toward the average (**expected value**).
The Central Limit Theorem prescribes that:

> The sum of a **sufficiently large number of samples** that are independent identically distributed random variables approximately follows a **normal distribution**.

The second strong feature of this measurement setup is the absolute amount of conducted measurements. Considering only turnouts with at least one measurement a week on average, yields a dataset with **sufficiently large number of samples**. This can be leveraged by applying the Central Limit Theorem which implies that the measurements of considered turnouts will be **normally distributed**. This statistical approach deals with the randomness and the shortcomings of the current measurement setup.

3.4.2. Measurement data exploration

In this thesis, the measurements from two trains of the same type are used. They have been driving their regular schedule without ProRail intervening. Therefore, it was not known a priori when or where these trains would run and under what conditions (e.g. route, speed). From the IM's perspective, the measurements where therefore conducted at random in space and time. The measurements are sectioned and mapped to track sections by the supplier. The raw dataset consists of approx. 18500 individual measurements distributed over 245 turnouts (in any direction or route over a 1:9 turnout). The measurement data content is shown in Table 3.1.

Table 3.1: Data content of individual measurements

Constants	Unit
Time stamp (UNIX)	s
Train	-
Train type	-
Continuous sigals	**Unit**
Time (UNIX)	s
Latitude, longitude (WGS84)	°
Running distance	m
Speed	km/h
Vertical acceleration (left, right)	m/s^2
Lateral acceleration (left, right)	m/s^2

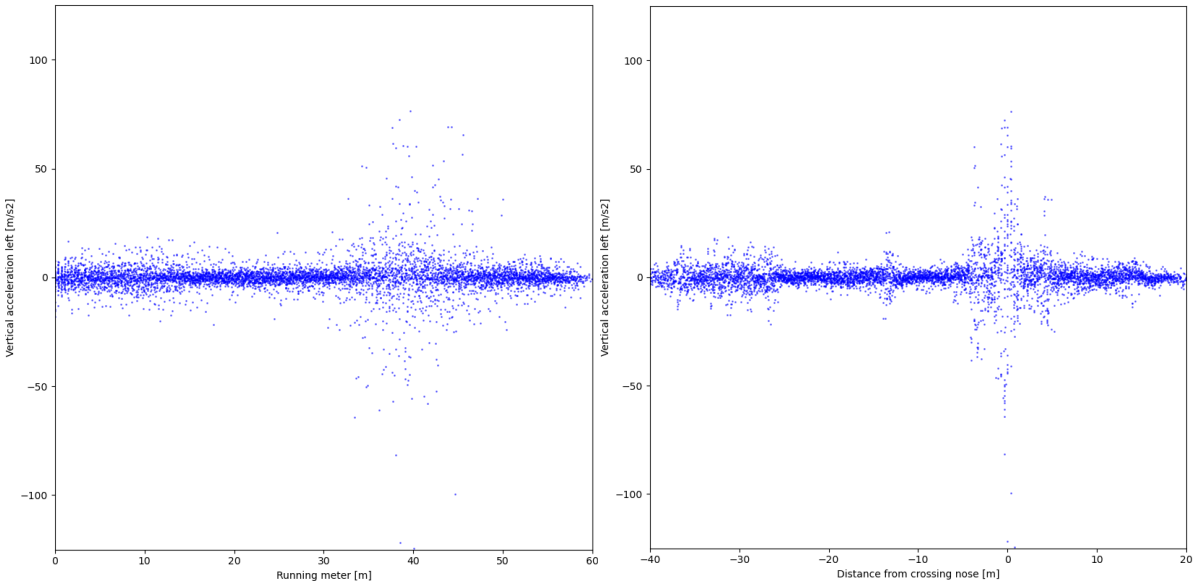

(a) Vertical accelerations (raw).

(b) Vertical accelerations (aligned on crossing impact).

Figure 3.7: Measurements (40) at a single turnout. Individual measurements are initially not properly aligned in longitudinal direction. Aligned measurements highlight signatures of different turnout components, i.e. switch blades (-30m), insulation joint (-13m) and crossing (0m).

A first inspection of the raw data is shown in Figure 3.7a. The vertical accelerations from multiple measurements are plotted against distance, where a distance of 0 m aligns with the front of the turnout according to the supplier. Although grossly the signatures of several turnout components are visible by plotting the raw data, the impact locations have a significant longitudinal spread lacking a localised crossing impact. This indicated that measurements are not mapped accurately to the infrastructure (i.e. the start of the measurement is not always on the same location). Since the impact on the crossing plays a major role in this thesis, an alignment algorithm is applied to locate the impact in each individual measurement. The origin of each measurement is shifted to the located impact location which aligns each measurement especially in the area of interest (near the impact on the crossing).

After aligning measurements (Figure 3.7b), which is elaborated in Section 3.4.3, the signatures of the turnout components become more pronounced and a clear and localised impact location becomes apparent. Analysis of the impact location of individual measurements yields the distribution as seen in Figure 3.8. This could be interpreted as a measure of initial mapping precision of the dataset. The distribution shows that the relative initial alignment can be off by ± 5m, with outliers up to 30m.

The outliers in Figure 3.8 gave reason to further inspect the underlying measurements. It was observed that measurements contained incorrect signals (Figure 3.9a) or could be lacking any impact (Figure 3.9b). There can be many factors that can lead to such signals, e.g. track allocation or sensor freezes handled in post-processing. However, the turnout that is taken as an example here, is located at one of the inner tracks within a section consisting of 4 parallel tracks. Most likely the measurement shown in Figure 3.9b was actually performed on the adjacent track, that does not contain a discontinuity (and thus no impact is measured). This suggests that the mapping algorithm of the supplier is not always correctly assigning measurements to the right track section.

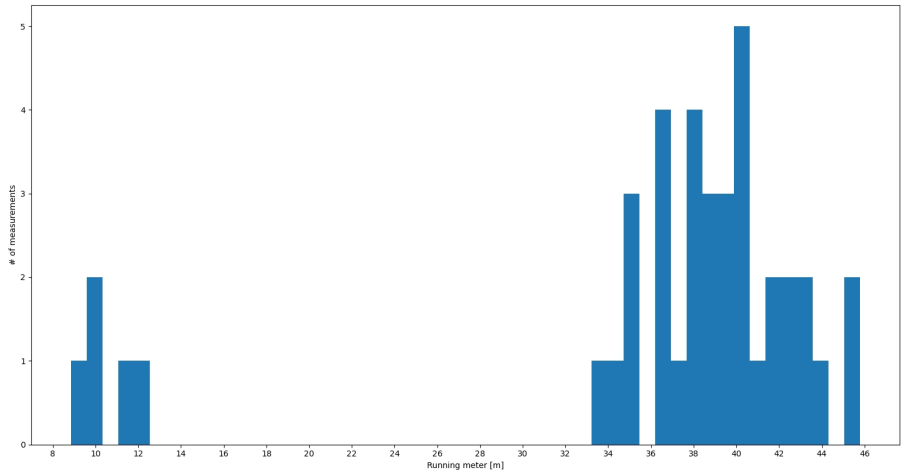

Figure 3.8: Detected impact locations with respect to the origin of the measurement. The crossing nose is located at +43.7 m.

3.4.3. Data cleaning

Section 3.4.2 showed that the raw dataset requires a check and cleanup to filter out faulty measurements and increase reliability. The raw dataset is subjected to the criteria shown in Table 3.2. The aim of these criteria is to filter out incomplete, corrupted or wrongly mapped measurements for the given turnouts. This yields a reliable dataset of approx. 5000 measurements divided over 38 turnouts. The distribution of measurements per turnout is shown in Figure 3.10. This ensures that further analysis is based on a dataset consisting of valid, realistic measurements that are under the scope of this thesis (see Section 1.5).

Table 3.2: Criteria set for each individual measurement.

Check	Threshold
# of data points	> 45
# invalid or missing values	< 20
Measurement duration (t)	$0.5 < t < 10$ s
Measurement distance (s)	$20 < s < 200$ m
Vertical impact amplitude	$10 < a_z < 160$ ms/s^2
Relative heading (w.r.t. the turnout)	$-10° <$ angle $< 10°$

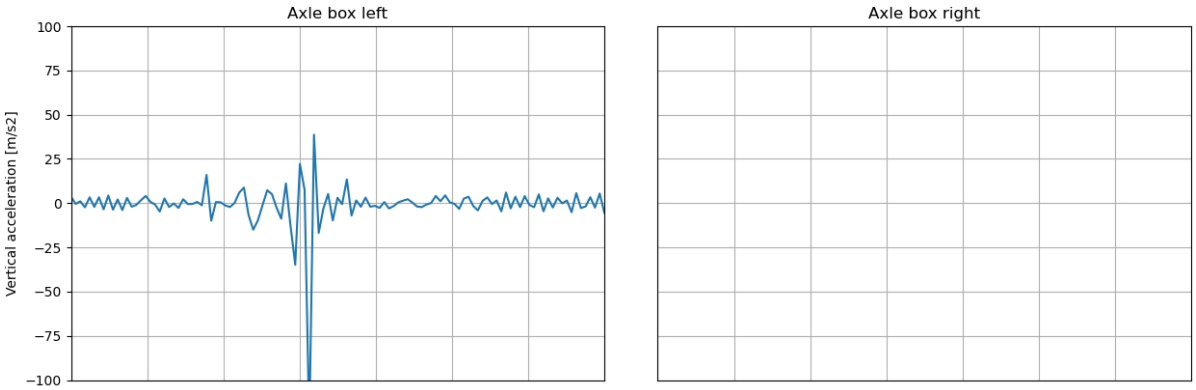

(a) A measurement with a corrupted signal (right).

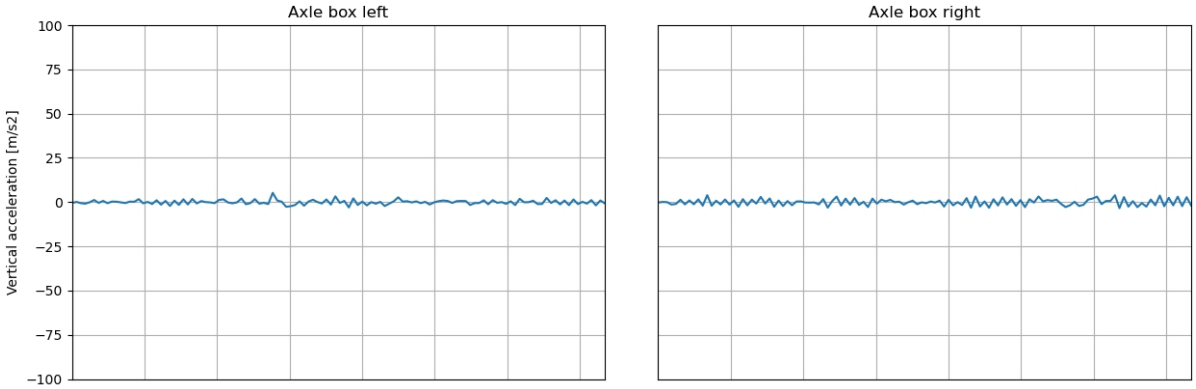

(b) A measurement that does not contain an impact.

Figure 3.9: Raw measurements with data quality issues.

3.5. Conclusion

SHM is a passive, operational variant of non-destructive testing. Under normal operational conditions (so during service life), the response of a structure is captured. A monitoring system for railways should at least be able to detect anomalies that can also be localised. However, the railway industry is relatively conservative. Manual (visual) inspection is still one of the foremost monitoring practices. The human factor makes judgement subjective and potentially erroneous. Therefore, monitoring systems based on physical principles have been developed. ABA is such a monitoring system that is based on vibrations. The monitoring system should be tuned to the expected frequencies and underlying dynamics. This can often be translated to a sufficiently high SF, given that the Sampling Theorem dictates that at the SF should be at least twice as high as the maximum frequency of interest.

ABA is relatively affordable and can easily be installed or retrofitted on trains. In-service passenger trains cover a large extent of the railway network and often multiple times a day. This makes in-service passenger trains a good candidate for this monitoring system, yielding information about the track state with small time intervals. However, this also introduces challenges with respect to data quality, quantity and processing. Furthermore, uncertainties are introduces since the measurements are conducted at random from the IM's perspective under random conditions (e.g. speed, loading, etc).

The current measurement setup of RaM is sub-optimal for the set goal of this thesis. The low SF limits the accuracy of the signal, and the current signal processing causes individual measurements to not be suitable for the set goal of assessing the crossing health. The underlying dynamics cannot be captured accurately, mainly due to the low SF. Future generations of this system could potentially overcome this limitation. However, the current setup requires to deviate from previous conducted studies where time-frequency analysis yield promising results. A statistical approach can deal with the current measurements, since the Law of Large Numbers supplemented by the Central Limit Theorem can leverage the strong features of the system: large amount of measurements with relative small intervals.

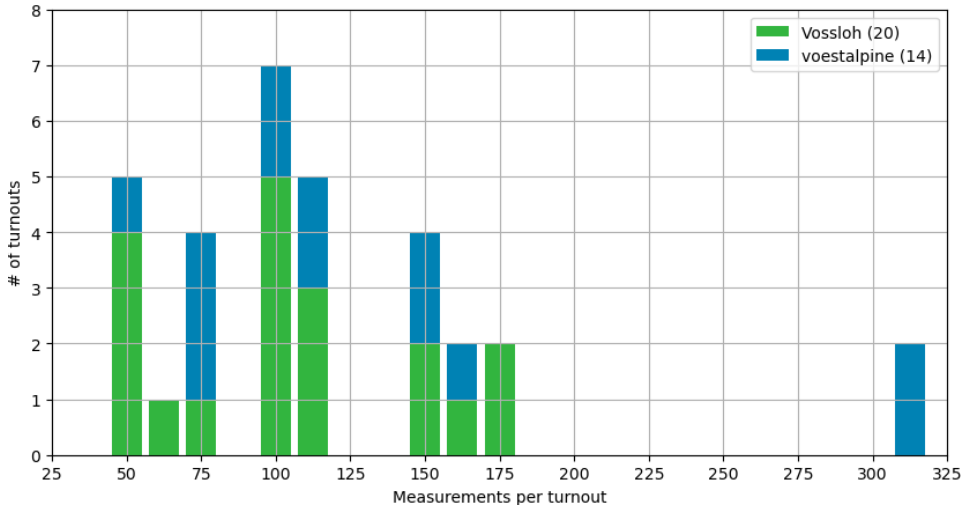

Figure 3.10: Distribution of measurements per turnout after data cleaning, categorised by manufacturer.

At this point an answer can be formulated to research sub-question 2:
"How should in-service passenger train ABA data be processed such that it accurately represents the crossing's structural health?"

Detection and localisation are minimal requirements for a feasible railway monitoring system. It can be challenging to accurately map measurements and guarantee high data quality. Therefore, measurements should be exposed to a basic quality check (is the data valid and complete?) and sanity check (does the data make sense?) and the processes implemented for this is understood prior to any further analysis, such as not to include data that is marked as invalid. Previous studies show that time-frequency analysis yield promising results. This requires a proper measurement setup, tuned for the involved dynamics and expected frequencies. Given the continuous measuring nature of in-service passenger trains, large amounts of data are generated. Also, the measurement conditions are not controlled (e.g. speed, loading). This is inherently different from dedicated measurement trains that can deal with large amounts of data more easily and measure in a controlled environment. If data compression by downsampling is unavoidable, the accuracy of describing the underlying dynamics is undermined and makes individual measurements unreliable. Utilising a statistical approach can deal with the inaccuracies introduced by downsampling but requires a significant amount of measurements.

4

Assessment

4.1. Feature distributions

The ABA measurements conducted are mapped to track sections by the supplier, after which they undergo a series of checks as described in Section 3.4.3. This yields a valid dataset with measurements that are linked to a turnout (and therefore grossly localised). The first processing step is to localise the impact and align the measurement accordingly, by setting the origin at the impact location. This ensures that all measurements are aligned with eachother, yielding an accurately localised dataset. All relevant features are extracted from each individual measurement, the considered features are listed in Table 4.1. The features from individual measurements form a distribution per turnout. An example of the feature distributions of the vertical and lateral impacts of a single turnout are visualised in Figure 4.1. A normal distribution is assumed for the features, as elaborated in Section 3.4.1.

Table 4.1: Features extracted from individual measurements.

Feature	Derived
Vertical impact	No
Lateral impact	No
Impact angle	Yes
Speed	No

The assessment of a crossing consists of two components:

- The vertical impact distribution as estimator for the vertical geometry
- The impact angle distribution as indicator for regular or irregular contact

The proposed assessment is based on the two characteristics that describe a normal distribution; the mean μ and the standard deviation σ. The mean vertical impact amplitude (μ_{vert}) is related to (degraded) vertical geometry. As demonstrated by Liu, 2020, an increase spread in vertical impact forces (σ_{vert}) is expected due to degraded vertical crossing geometry. A similar effect can be expected from train-borne measurements. The mean impact angle μ_{alpha} (see Figure 2.4) indicates if the contact is predominantly regular or irregular. The spread σ_{α} indicate the consistency of contact situations. A large spread in contact situations suggests that passing trains are excited laterally, which can be caused by e.g. bad track/turnout geometry.

To link the features to degradation, two validation steps are conducted. First, a correlation analysis is done to rule out (dynamical) effects embedded in the ABA data that is not accounted for in Chapter 2. Secondly, a correlation analysis is conducted to quantify the ability of describing degraded vertical and lateral geometry. Lastly, case studies are conducted to confirm relations found by the correlation analysis.

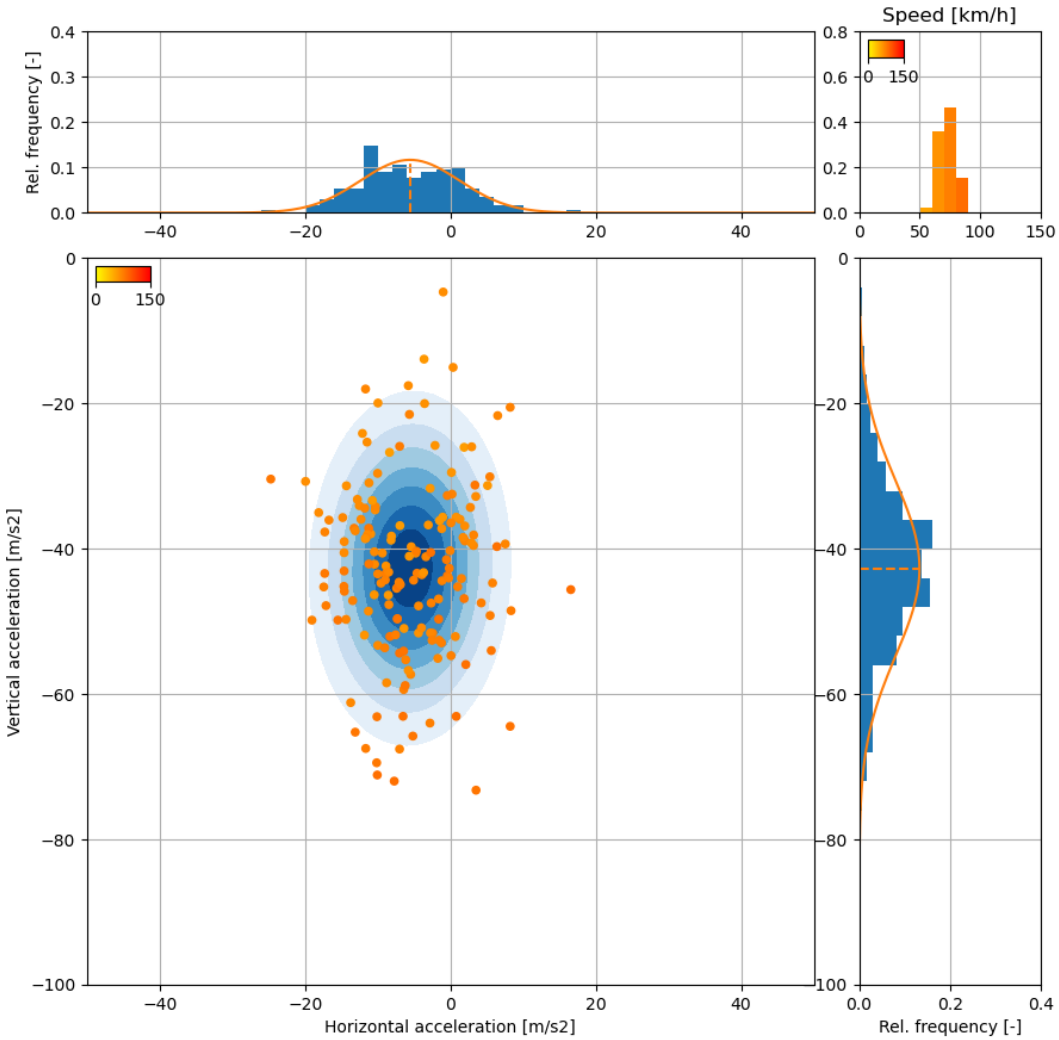

Figure 4.1: Visualisation of vertical and lateral impact distributions of turnout 10101187. The impact from a single measurement is represented by a dot. The colour indicates the speed during the measurement, which corresponds to the the speed distribution of all measurements in the top right corner.

4.2. Correlation analysis

4.2.1. Correlation levels

The Pearson correlation coefficient is the most common used measure of linear association. It is often referred to as ”correlation” or ”correlation coefficient” to quantify relationships between different continuous variables. The correlation coefficient is defined as

$$r = \frac{SS_{xy}}{\sqrt{SS_x SS_y}}$$

Where r is the Pearson correlation coefficient, SS_x the sum of squares of x, SS_y the sum of squares of y and SS_{xy} the sum of squares of x and y (Boslaugh, 2012). Many real-world variables appear to be associated by having a strong correlation. However, correlation is a measure of observed relationship, but does not prove causation. Proving causation of variables with high correlation requires more explanation by experimental setups and/or modelling, which is a major element of science. Scatter plots

like are created to visualise these relationships (Boslaugh, 2012). The Pearson coefficient has a range of (-1,1) where 0 indicates that there is no relationship. The larger $|r|$, the stronger the relationship between the variables. Calling a relation "strong" does not have strict scientific definitions. Often a field of study has conventions for this to establish a framework for comparison. Since similar effects as measured by wayside measurements are expected from vehicle-borne measurements, the same correlation levels of Liu, 2020 are used in this thesis. The definitions are specified in Table 4.2. The correlation can be misleading if the data has a non-linear relationship which is why understanding the underlying physics and data visualisation is important.

Table 4.2: Correlation strength definitions

Correlation coefficient			Label
	$\lvert r \rvert$	< 0.3	Weak
$0.3 \leq$	$\lvert r \rvert$	< 0.5	Moderate
	$\lvert r \rvert$	≥ 0.5	Strong

4.2.2. Hidden side effects

In Table 4.3 and Table 4.4 the correlations between several features are shown. Both crossing types show a strong correlation between μ_{vert} and σ_{vert}. This can be interpreted as degraded geometry (large impact forces) leading to a wider variety of impact amplitudes. This is in agreement with the findings of Liu, 2020 based on way-side monitoring of crossings. However, this most likely is an undesired side-effect of the block averaging of the measurements, i.e. the absolute error (reflected in σ_{vert}) increases for larger impacts assuming a fixed relative error (see Section 3.3.2). Moreover, there is a strong correlation between μ_{alpha} and μ_{lat}. This is expected given the definition of alpha in Figure 2.4, where the lateral component predominantly determines the angle. Lastly, there is a weak correlation between μ_{vert} and μ_{speed}. Initially this may look like a flaw, given the relation between speed an the vertical impact elaborated in Section 2.2.3. However, this stipulates that a vertical impact is the product of the measurement speed and the vertical geometry. A good vertical geometry can yield lower impacts at high speed and a bad vertical geometry can yield high impacts at low speed.

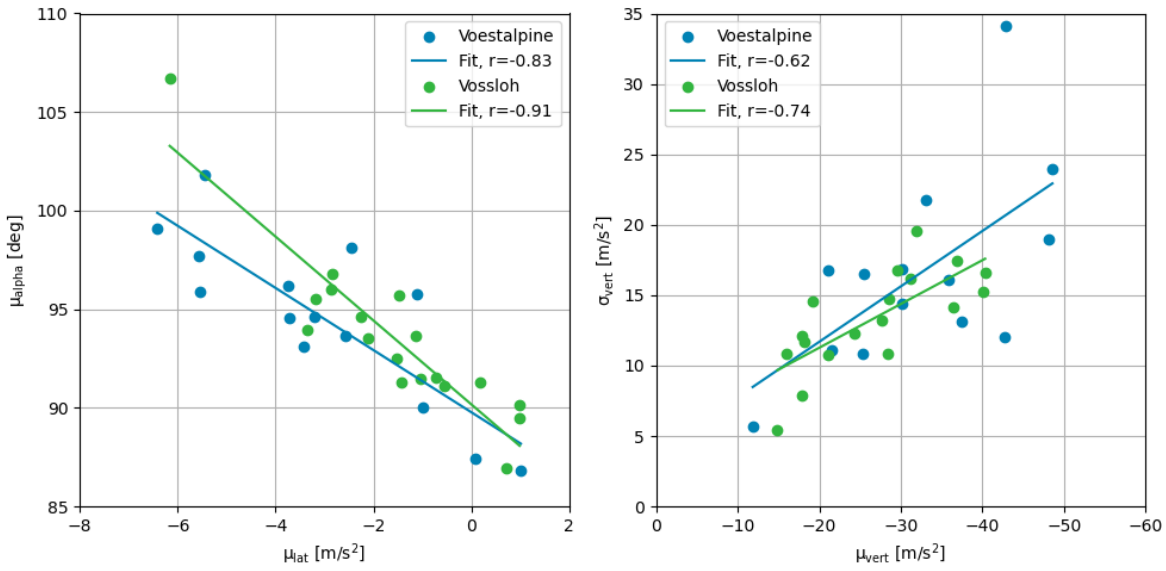

Figure 4.2: Features with strong correlations between each other.

However, there are two discrepancies between the crossing types. It concerns the correlation of μ_{speed}-μ_{lat} and μ_{speed}-μ_{alpha}, which the underlying data is shown in Figure 4.3. There are significant different correlations between μ_{speed} and μ_{lat}. A possible explanation is that Vossloh applies elevated wing rails. From the data, it suggests that this modification alters the wheel-rail dynamics such that the wheelset is forced laterally towards the crossing nose. It appears that at higher speeds this force increases. However, this effect is not further studied in this thesis. The second discrepancy is the stronger relation between μ_{speed} and μ_{alpha} in the case of Vossloh. However, given the strong correlation between μ_{lat} and μ_{alpha} this is the same effect as the prior one, in a different representation. The outliers are studied in-depth in case studies.

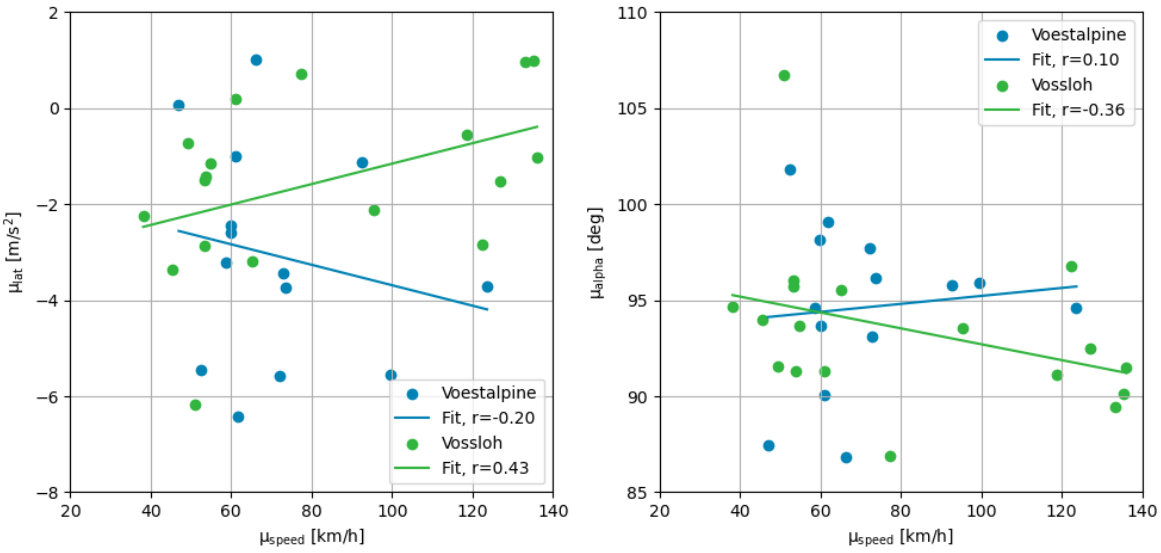

Figure 4.3: Discrepancies in correlations between the two crossing designs.

Table 4.3: Correlation coefficients for Voestalpine crossings.

r	μ_{vert}	σ_{vert}	μ_{lat}	μ_{speed}	μ_{alpha}
μ_{vert}	1	-0.62	0.24	0.19	0.09
σ_{vert}		1	-0.19	0.28	-0.06
μ_{lat}			1	-0.20	-0.83
μ_{speed}				1	0.10
μ_{alpha}					1

Table 4.4: Correlation coefficients for Vossloh crossings.

r	μ_{vert}	σ_{vert}	μ_{lat}	μ_{speed}	μ_{alpha}
μ_{vert}	1	-0.74	0.17	0.07	0.10
σ_{vert}		1	0.11	0.19	-0.29
μ_{lat}			1	0.43	-0.91
μ_{speed}				1	0.36
μ_{alpha}					1

4.3. Irregular contact

Section 2.2.2 elaborates on the relation between impact angle (indicating irregular contact) and the relation to wear. In Figure 4.4 the impact angle features are correlated to the absolute crossing nose wear. μ_{alpha} shows for both crossing types a moderate but opposite signed correlation. The impact angle model elaborated in Section 2.2.2 expects a negative relationship between μ_{alpha} and the crossing nose wear (small μ_{alpha} should lead to the most crossing nose wear). Therefore it is remarkable that the Vossloh crossing seems to have a positive relationship. σ_{alpha} seems not to be correlated to the absolute wear levels. The same analysis is done for wing rail wear, seen in Figure 4.5. μ_{alpha} shows no relation with the absolute wear levels. σ_{alpha} suggests a strong correlation for the Voestalpine crossings, however given that there appears not to be a relation in the case of μ_{alpha}, this is considered as incorrect.

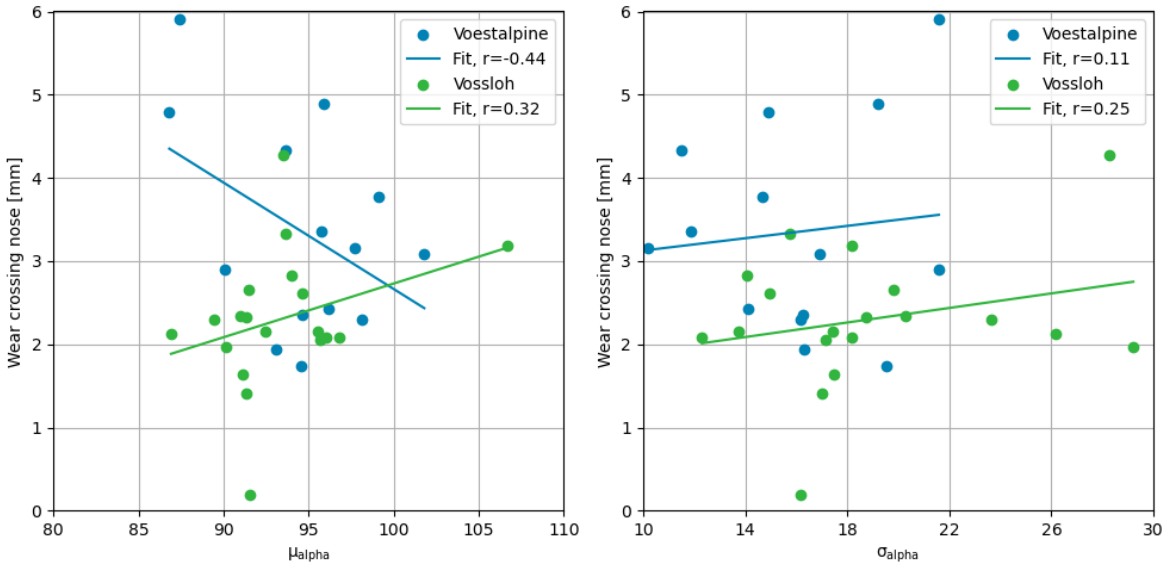

Figure 4.4: Correlation between the impact angle features and absolute wear on the crossing nose.

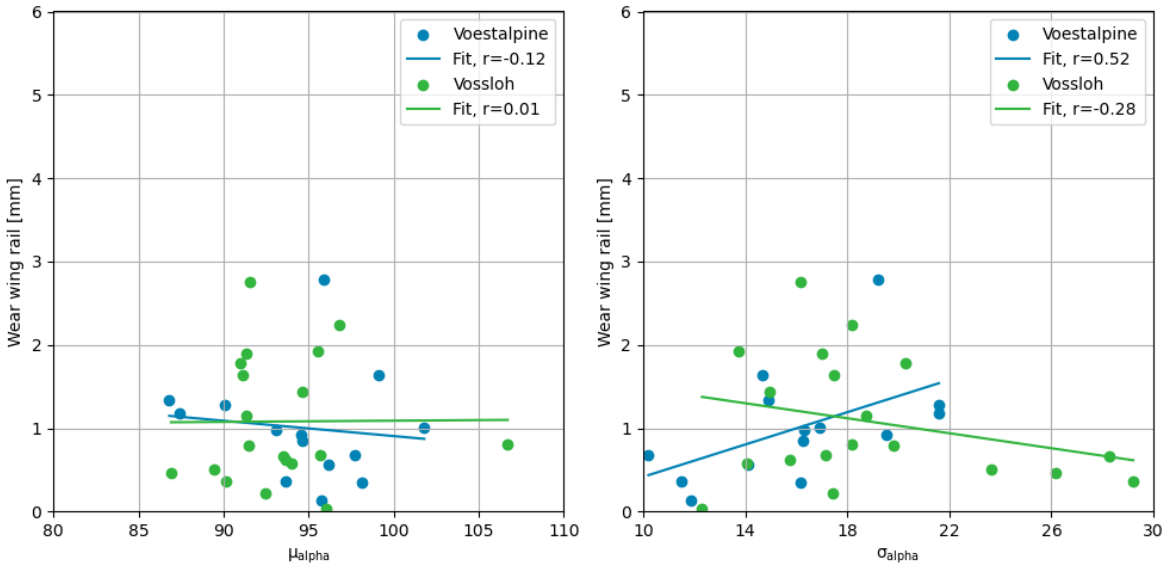

Figure 4.5: Correlation between the impact angle features and absolute wear on the wing rail.

The service life of a crossing is generally much larger than the ABA measurement period of approximately one year. The condition of the whole turnout and neighbouring track is not stationary due to deterioration and maintenance. Therefore, the absolute wear is the product of a longer time period. The wear generated during the ABA measurement period could therefore be considered instead, which can be determined from two consecutive laser measurement campaigns. Therefore, the first campaign (March 2022) is related to crossing condition in the beginning of the ABA measurement period, the last campaign (September 2022) to the condition towards the end of the ABA measurement period. The correlations between the impact angle features and the wear generated during the measurement period can be found in Figures 4.6 and 4.7. The general picture as for the correlations with absolute wear does not significantly changes. μ_{alpha} shows a strong and moderate but opposite signed correlation. However, looking at the underlying data, the correlation is not reliable.

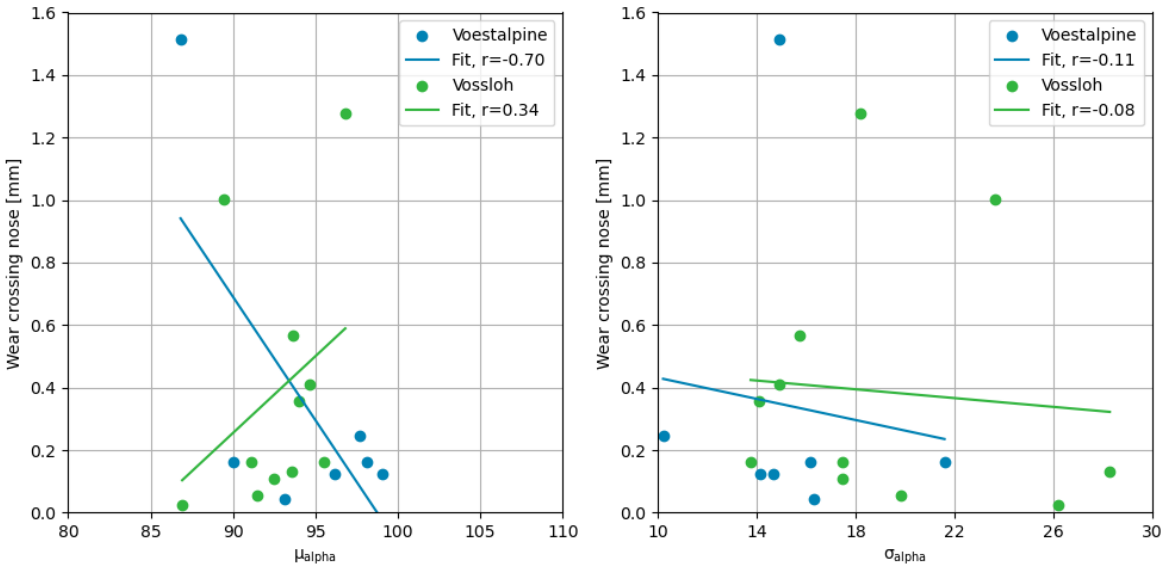

Figure 4.6: Correlation between the impact angle features and relative wear on the crossing nose.

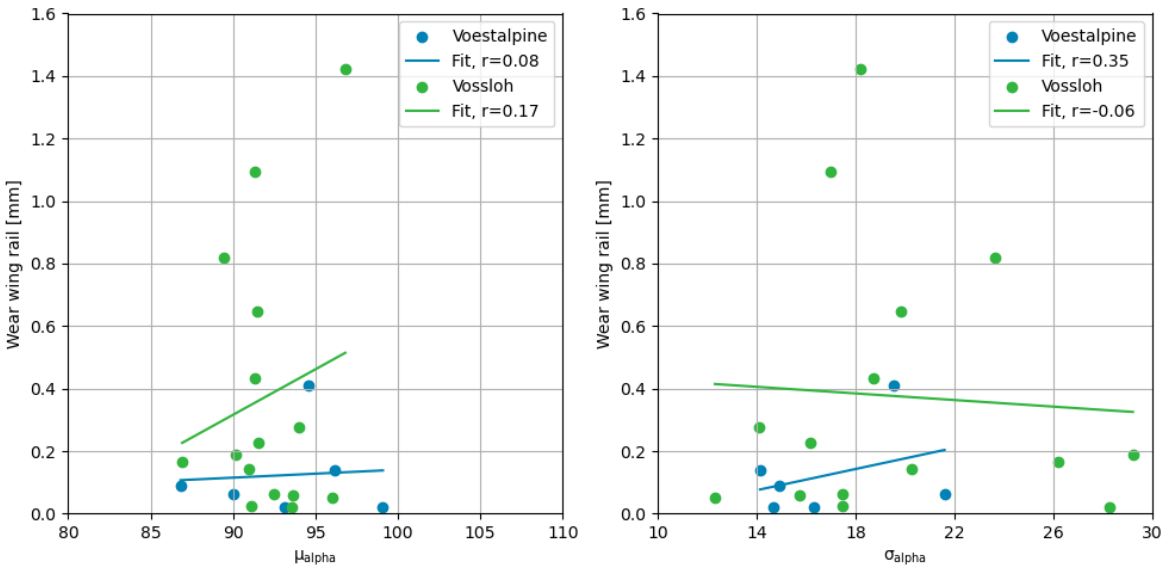

Figure 4.7: Correlation between the impact angle features and relative wear on the wing rail.

A last relationship is searched for by categorising individual measurements by impact scenario, as defined in Figure 2.4. The category definitions can be found in Table 4.5. All measurements are now distributed over these contact scenarios. From Section 2.2.2 can be derived that a high relative occurrence of scenario B should be related to wear on the crossing nose, whereas a high relative occurrence of scenario C should be related to wear of the wing rail. In Figure 4.8 these expectations are not reflected. There are not relations found, the only strong correlation is not fitting the underlying data well, making a relationship unlikely.

Table 4.5: Definitions of impact scenarios, related to Figure 2.4.

Contact scenario	Impact angle
A - regular	$85° <= \mu_{alpha} <= 95°$
B - inner flange - crossing nose	$\mu_{alpha} > 95°$
C - flange back - wing rail	$\mu_{alpha} < 85°$

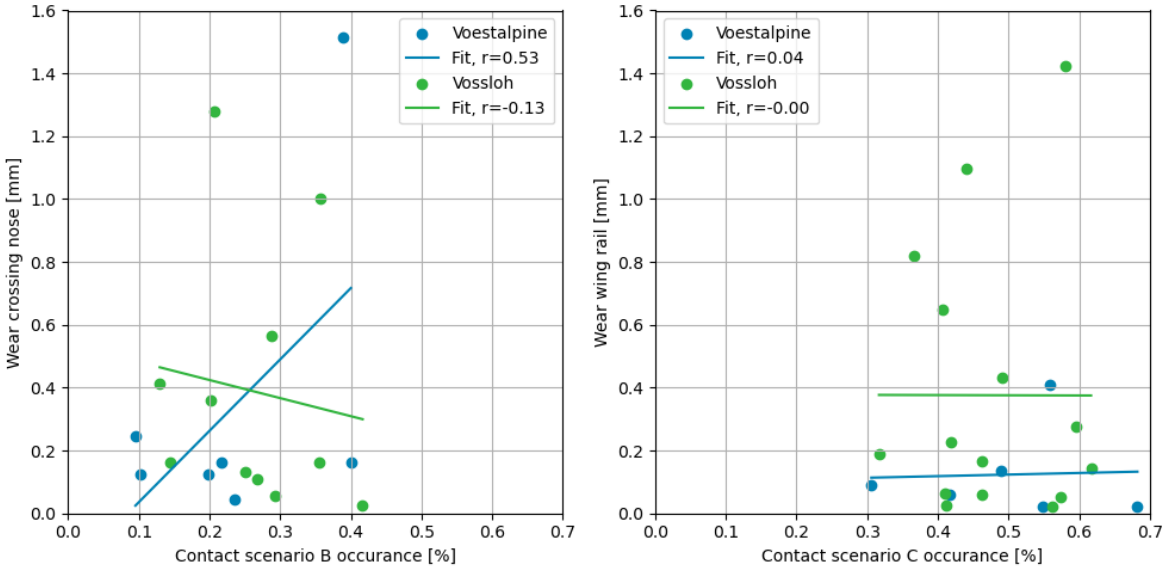

Figure 4.8: Correlation between occurrence of contact scenarios and measured increase of wear in half a year.

There is a discrepancy between the expected relationships and absence of relationships in the correlation analysis. Therefore, the validation data (derived wear levels from the laser geometry data) was investigated. Although the exact inner working is not studied, the general principle of determining wear levels is calculating the difference between fitted nominal geometry and the measured geometry. However, the nominal geometry fit of especially the crossing nose is not always accurate, leading to overestimating the wear level. An example can be seen in Figure B.1. The nominal crossing nose geometry on the considered through route is visualised by the blue line, where the blue value indicates the magnitude and location of the maximum wear level. Subjectively, the shape of the crossing nose is close to the nominal state. The nominal crossing nose fit overshoots the linear part of the crossing nose, leading to an artificial wear maximum at the top of this fit. This adds significant noise to the validation data, which is part of the reason no reliable relationships are found.

This effect is not dominantly present in the case of the wing rail due to the more consistent cross-sections of the wing rail (and thus better nominal geometry fits). In this case, most likely the ABA measurements are not accurate enough due to the low SF. The speed of all measurements ranges from 40 to 140 km/h (11.11 to 38.89 m/s). With the current measurement setup with a SF of 104 Hz, the travelled distance represented by a single data point varies between 10 and 40 cm. Therefore, all involved dynamics are reduced to 1 or 2 data points. This is a gross approximation, most likely leading to inaccurate impact angle determination and thus an inaccurate representation of the contact situation. Moreover, the effect of check rail contact is assumed to be gentle with respect to the impacts, and therefore assumed to be accounted for in the contact scenarios. This assumption is not validated.

4.4. Vertical geometry

4.4.1. Wheel dip angle correlation

The vertical geometry and following vertical impacts can be estimated by the kinematic wheel dip angle β, as elaborated in Section 2.2.3. Based on laser scan geometry measurements performed by dedicated measurement trains, relevant parameters can be derived as shown by e.g. Wegdam, 2021. Utilising the geometry analysis from this study as elaborated in Appendix B, derived quantities like the kinematic wheel dip angle can be determined. The kinematic wheel dip angle is based on a perfectly centre trajectory and functions as dynamic impact force estimator, which in turn is an indicator for the vertical geometry.

In Figure 4.9 μ_{vert} and σ_{vert} are plotted against the corresponding kinematic wheel dip angle. There is a strong negative relation between the wheel dip angle and the mean impacts. This implies that larger measured impacts (in an absolute sense), results in larger wheel dip angles. This is in agreement with the studies referenced in Section 2.2.3. Moreover, there is a seemingly different relation between the two different crossing types. A possible explanation for this difference can again be found in a subtle differing wing rail for the two crossing types. Vossloh elevates the wing rail to reduce the vertical downward displacement of the wheel during stage 2. During stage 2 from Figure 2.3 the wheel experiences a downward vertical motion of the wheel due to the laterally displacing contact point towards to field side (the rolling radius reduces due to conicity). The elevated wing rail influences the wheel-rail dynamics and therefore impact forces. A moderate-strong relationship is found for the spread in vertical impacts, which was also observed by wayside measurements conducted by Liu, 2020. There is an outlier at $\sigma \approx 34$, which will be studied more in depth as a case study.

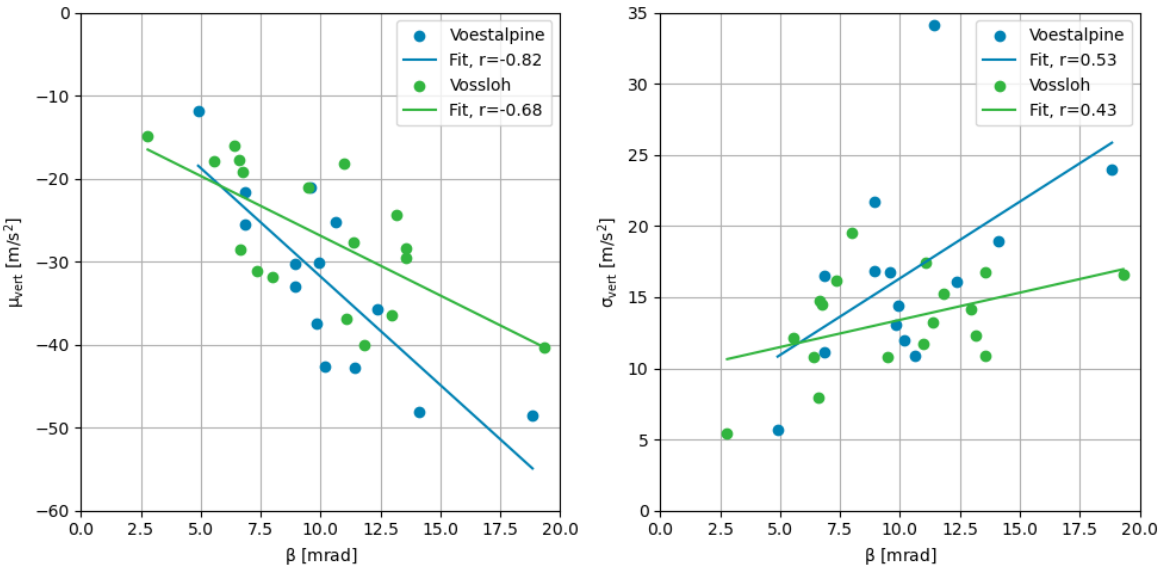

Figure 4.9: Correlation between vertical impact distribution characteristics of individual turnouts and the kinematic wheel dip angle, derived from measured turnout geometry.

4.4.2. Case studies

In Figure 4.10 a couple extremes are specifically marked. According to the assessment approach, these turnouts are among the most degraded crossings. Turnout 11514060 stands out by both the large μ_{vert} and σ_{vert}. The defect registration database of this turnout showed that on 01-11-2022 (one month prior to the end of the measurement period) the crossing nose was ruptured. A picture taken by a technician is shown in Figure 4.11a. This confirms that a large measured μ_{vert} corresponds to severe degradation or even sudden failure in this case.

Turnout 10120776 has a similar μ_{vert} magnitude as the previous turnout. No replacement or failure is reported, however on 09-08-2022 the contractor decided to do maintenance on the crossing nose, which was reported as grinding the crossing nose. This indicates that there was an incentive to do maintenance. The geometry laser measurement from February 2022 shows a heavy worn crossing nose profile (5 mm difference with respect to nominal geometry), indicating wear and plastic deformation. This observation corresponds to the relative wide running band on the crossing nose, seen in Figure 4.11b.

Turnout 10120755 shows the largest σ_{vert} in the dataset. A report states that maintenance is conducted on 01-09-2022, however it is not specified what is exactly done. Figure 4.12a shows a large spread in vertical impact amplitude prior to the maintenance, while the impacts after maintenance show a more consistent pattern. This causes the acceleration distribution to not be normally distributed, instead consisting of two independent distributions with differ in mean and standard deviation (originating from the degraded situation and new situation). σ_{vert} becomes very large if the data is considered as a single distribution. In the context of Figure 4.10, the derived features of this turnout could be considered as outliers.

Lastly, turnout 11503857 did not receive any maintenance according to the official registration. The geometry measurements show a heavily worn crossing nose profile. The contact transition zone in the surface picture in Figure 4.11c appears to be extremely short, which hints to a large impact. This is also reflected in the magnitude of β. The significant degradation on this crossing nose is remarkable given that the crossing was installed in August 2020, thus having a service life of just two years .

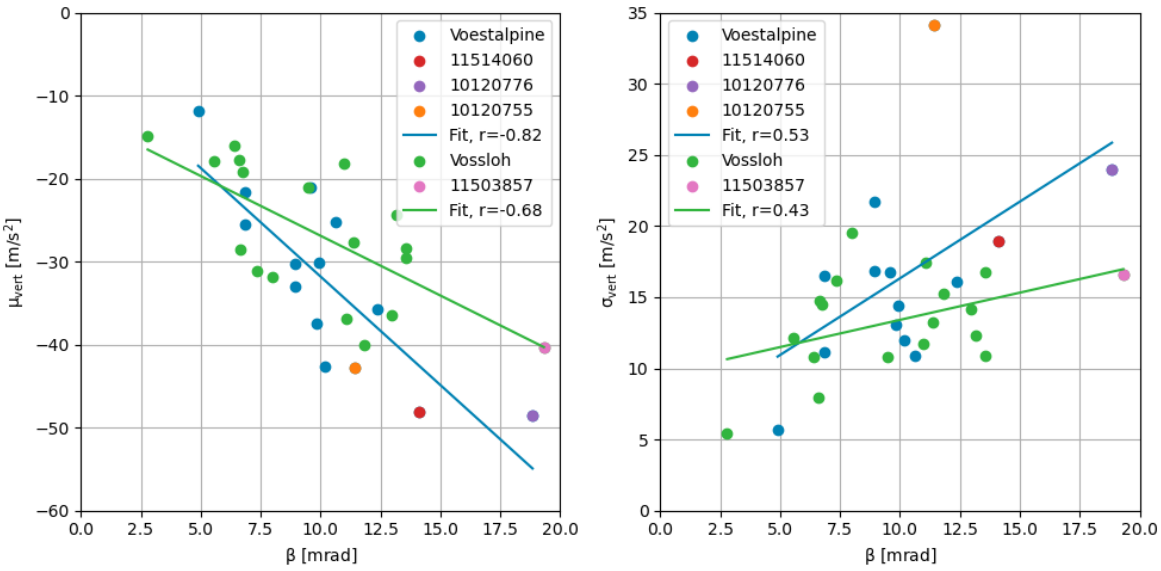

Figure 4.10: Turnouts with extreme values.

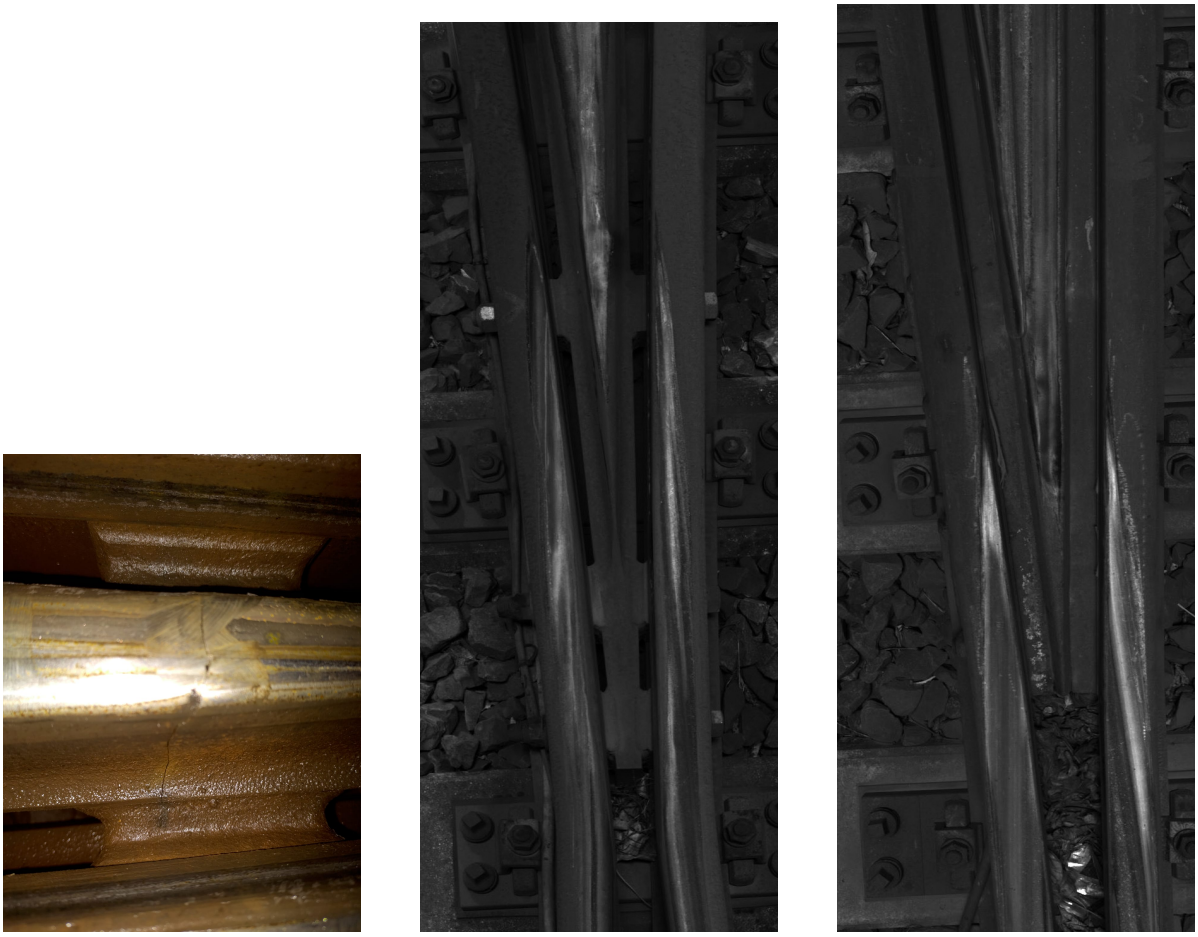

(a) A ruptured crossing nose on turnout 11514060.

(b) Top view of the crossing of turnout 10120776. Picture taken in May 2022.

(c) Top view of the crossing of turnout 11503857. Picture taken in June 2022.

Figure 4.11: Pictures of considered crossings in case studies.

4.5. Conclusion

Proper alignment of measurements enable reliable feature extraction, which in turn is essential for the proposed statistical approach. The vertical impact distribution and impact angle distribution are the features of all measurements of a single crossing are taken into consideration. The proposed assessment is based on the two characteristics that describe a normal distribution: the mean and standard deviation. By means of a correlation analysis, the method is validated against geometry metrics derived from train-borne laser measurements (see Appendix B). The Pearson coefficient is used as a measure of observed relationship.

First, a correlation analysis is conducted among the features to highlight any hidden effects, embedded in the dataset. No anomalies were found except for a discrepancy in behaviour between the two crossing manufacturers. A possible explanation is the altered wheel-crossing dynamics due to the elevated wing rail, however this is not further studied in this thesis. This concludes that from a statistical point of few, there are no (strong) hidden dependencies in the dataset that is not accounted for.

The impact angle features μ_{alpha} and σ_{alpha} were expected to be related to wear levels on the crossing nose and wing rail. Based on geometry laser measurements these wear levels were determined. Also the wear generated during the ABA measurement period specifically is considered. However, the current approach does not yield any (reliable) relationship between the impact angle and wear levels. Therefore, the current approach is not suitable for monitoring wear levels.

There is a strong relation for both crossing types between μ_{vert} and β. This implies that the measured dynamic impact amplitude is strongly related to bad vertical geometry, which was expected from the vertical dynamics studied in Section 2.2.3. Therefore, μ_{vert} can be used as indicator for the longitudinal-vertical geometry. Moreover, case studies show that the largest impact amplitudes correspond to heavily degraded crossings or failed crossings. Therefore, with current assessment approach, based on the current measurement setup, the vertical geometry can be well assessed. Based on the conducted studies, μ_{vert} > 40 m/s^2 is considered as heavily degraded crossing. No clear degradation thresholds are found for σ_{vert}, however the heavily degraded crossings also had the largest σ_{vert}. It can therefore be used in a relative sense, e.g. for prioritising maintenance.

Now, an answer can be formulated to research sub-question 3:
"What is a suitable method to identify degradation of individual crossings based on in-service passenger train ABA?"

> Aligned measurements are required for reliable feature extraction. A statistical approach by considering the distribution of vertical impacts can be taken, based on many measurements. By means of correlation analysis, relationships can be found between features and properties derived from geometry laser measurements. A strong relationship between the kinematic wheel dip angle and μ_{vert} was found. Therefore, the vertical geometry can be assessed by the magnitude of μ_{vert}, where a larger μ_{vert} means a more degraded vertical geometry. Heavily degraded crossings are found for μ_{vert} > 40 m/s^2. σ_{vert} showed a strong correlation with kinematic wheel dip angles. A larger σ_{vert} therefore is linked to more degraded geometry. This is in line with wayside observations from other studies. However, no clear threshold is found to regard a crossing as heavily degraded. Therefore, this feature specifically can be used in a relative assessment of multiple crossings in case of e.g. prioritising maintenance.

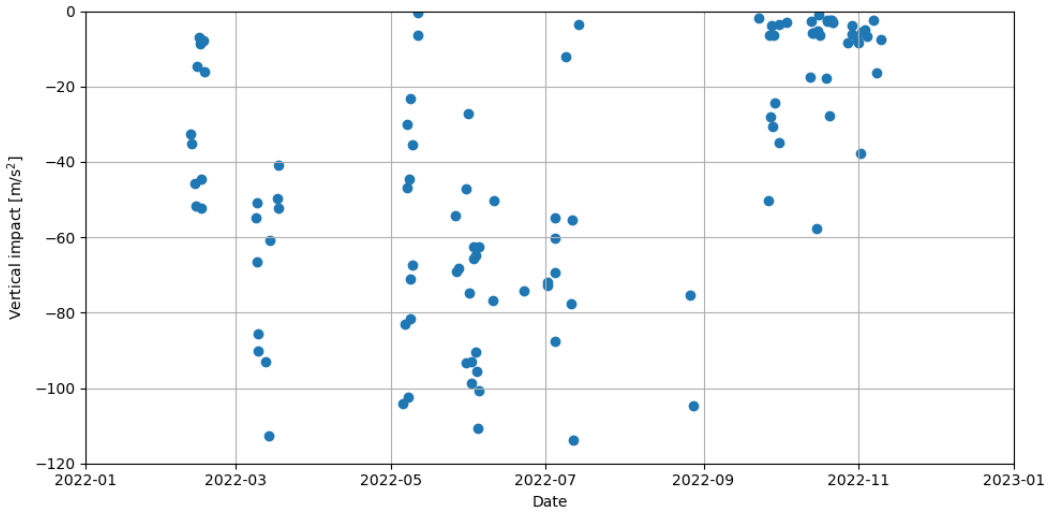

(a) Impacts that show a different behaviour after 01-09-2022.

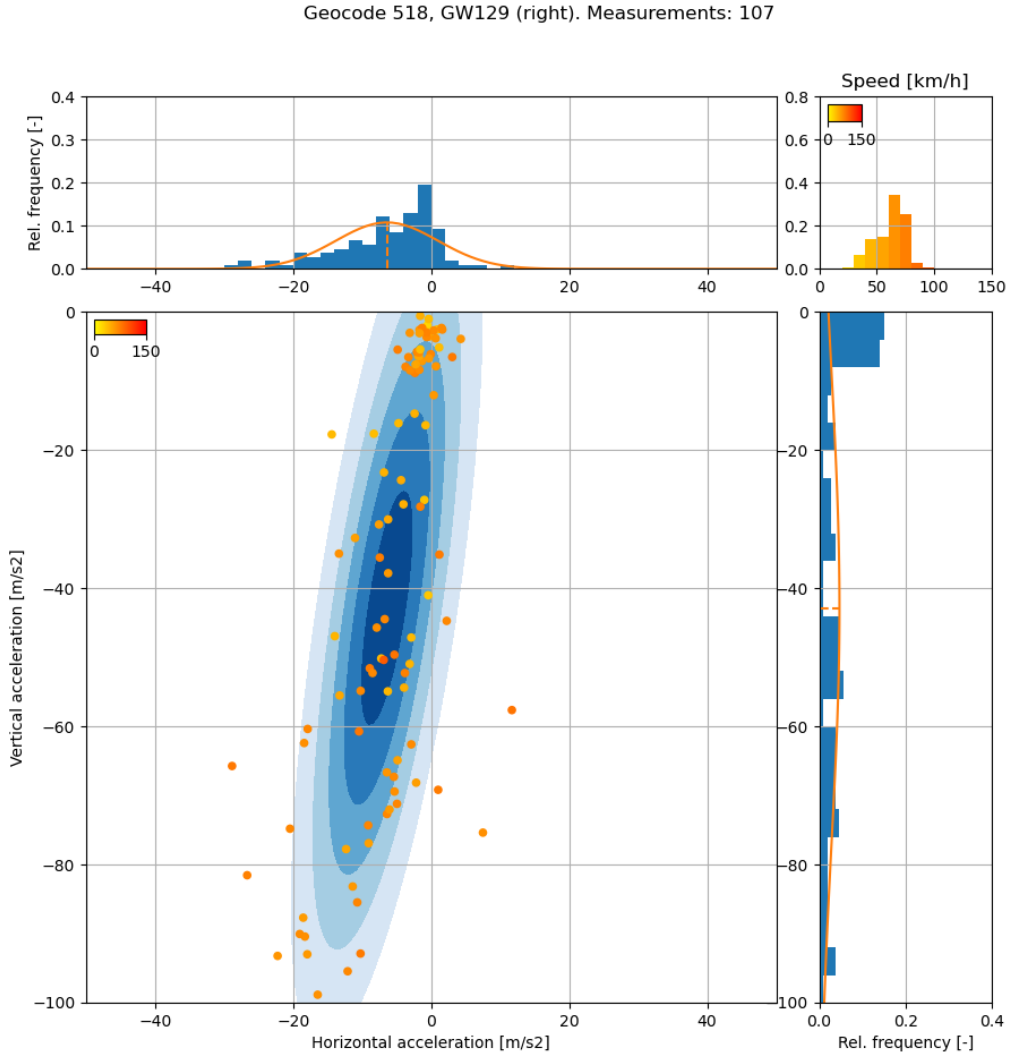

(b) Impact distribution that is not normally distributed.

Figure 4.12: Measurement data of turnout 10120755.

5

Conclusions and recommendations

5.1. Conclusion

In Section 1.3 the research objective is defined, leading to the research question defined in Section 1.4. To answer the research question, sub-questions have been formulated that are answered in the previous chapters:

- *Q1 What are the degradation mechanisms of crossings? (Chapter 2)*
- *Q2 How should in-service passenger train ABA data be processed such that it accurately represents the crossing's structural health? (Chapter 3)*
- *Q3 What is a suitable method to identify degradation of individual crossings based on in-service passenger train ABA? (Chapter 4)*

By answering the sub-questions, an answer to the main research question can be formulated:

How can in-service passenger train Axle Box Accelerations (ABA) be utilised to assess the structural health of a turnout crossing?

> The crossing of a turnout is subjected to severe wheel-rail contact due to the transition of contact from wing rail to the crossing nose. This transition is the driving force behind three degradation mechanisms: plastic deformation, RCF and wear. The degradation mechanisms are related to the dynamic forces resulting from the transition. These dynamics can be measured by ABA, a vehicle-borne monitoring system. It is challenging to accurately map ABA measurements, therefore quality checks and (alignment) corrections should be applied to guarantee high data quality. Moreover, the measurement setup should be tuned for the involved dynamics and expected frequencies. ABA is well-suited to retrofit on in-service passenger trains that cover a large extend of the network on a daily basis, thus yielding a accurate insight of the infrastructure condition due to the relatively short measurement intervals. Continuous measurements by in-service trains generate large amounts of data, therefore a trade-off between accurately capturing the dynamics and data reduction is made. The reduced accuracy potentially renders single measurements unreliable. Application of statistical concepts deals with the introduced inaccuracies but requires a large amount of individual measurements. Impacts derived from aligned ABA measurements form a normal distribution, which can be described by the mean and standard deviation. These properties can be used as features to assess the condition of a crossing. An assessment based on impact angles does not yield useful insights in the current context. However, the mean vertical impact has a strong relation to the vertical geometry. A larger mean vertical impact relates to a more unfavourable vertical geometry. Thereby, the condition of an individual turnout crossing can be assessed based on in-service passenger train ABA.

5.2. Recommendations

During this research, several shortcomings and/or drawbacks have been identified leading to the following recommendations:

- The scope of the current measurement setup should be evaluated. For reproducing long-wave track parameters the current setup is suitable, judging by the specifications (not verified). However, the current setup filters out relevant information about impact-related dynamics. Scientific publications show a large potential in utilising time-frequency analysis based on ABA as monitoring platform. But this requires a sufficiently high SF. To utilise the full potential of this system on the Dutch railway network (max. speed 140 km/h), a SF of 7.5 kHz is advised, with 2.5 kHz as bare minimum. At top speed, these SF are able to detect defects of 1 cm and 3 cm respectively, covering most occurring short-wave rail defects. On lower speeds, sub-centimetre defects are detectable.
- Any analysis is dependent on reliable data. In the context of ABA, only accurate localisation allows individual measurements to be manipulated or compared. Inaccurate mapping of individual measurements to the physical track will yield unsatisfactory results per definition (the famous saying in computer science for this is ”garbage in = garbage out”). Efforts should be made to have a good alignment/mapping by default. Consistent alignment below half a meter accuracy would be considered good enough in this context.
- For regular or large scale analysis retrieving relevant data should be straight-forward and facilitated to not waste resources. To enable useful analysis and/or stimulate research, an Application Programming Interface (API) or direct database access is very much desired.

5.3. Future work

This thesis lays the foundation of a different approach of assessing railway infrastructure using in-service passenger train ABA. However, improvements can be made:

- The assumption of features being normally distributed not always correct due to replacements and maintenance. The accuracy of this method could be improved to detect different measured behaviour and accounts for this.
- Instead of a fixed measurement window (consider all data in a period), a moving window approach (consider a certain moving time frame) could potentially yield continuous condition assessment.
- The diverging route is not considered in this thesis. However, an similar assessment could be investigated for turnouts that are driven often on the diverging route.
- Fixed cast crossings were not considered in this thesis, these can be assessed using the same approach.

References

Boslaugh, S. (2012). *Statistics in a nutshell* (2nd ed.). O'Reilly Media.

Central limit theorem. (2008). In *The concise encyclopedia of statistics* (pp. 66–68). Springer New York. https://doi.org/10.1007/978-0-387-32833-1_50

Esveld, C. (2001). Modern railway track.

Gackowiec, P. (2019). General overview of maintenance strategies – concepts and approaches. *Multidisciplinary Aspects of Production Engineering*, *2*(1), 126–139. https://doi.org/doi:10.2478/mape-2019-0013

Jenkins, H., Stephenson, J., Clayton, G., Morland, G., & Lyon, D. (1974). The effect of track and vehicle parameters on wheel/rail vertical dynamic forces. *Railway Engineering Journal*, *3*(1), 2–16.

Johansson, A., Pålsson, B., Ekh, M., Nielsen, J. C., Ander, M. K., Brouzoulis, J., & Kassa, E. (2011). Simulation of wheel–rail contact and damage in switches & crossings [Proceedings of the 8th International Conference on Contact Mechanics and Wear of Rail / Wheel Systems, Florence, 2009]. *Wear*, *271*(1), 472–481. https://doi.org/https://doi.org/10.1016/j.wear.2010.10.014

Kruse, T. ((2022). *Reizigerstrein als Meettrein (RaM), Presentatie Infrabel* (tech. rep.). ProRail.

Law of large numbers. (2008). In *The concise encyclopedia of statistics* (pp. 297–299). Springer New York. https://doi.org/10.1007/978-0-387-32833-1_50

Li, Z., Molodova, M., Núñez, A., & Dollevoet, R. (2015). Improvements in axle box acceleration measurements for the detection of light squats in railway infrastructure. *IEEE Transactions on Industrial Electronics*, *62*(7), 4385–4397. https://doi.org/10.1109/TIE.2015.2389761

Liu, X. (2020). *Development of Condition Monitoring System for Railway Crossings: Condition Assessment and Degradation Detection for Guided Maintenance* (Doctoral dissertation). Delft University of Technology. Delft University of Technology. https://doi.org/10.4233/UUID:AADBB312-4596-4072-86F3-B43B3532AB40

Massel, A. (1999). Power spectrum analysis—modern tool in the study of rail surface corrugations. *NDT&E International*, *32*(8), 429–436. https://doi.org/https://doi.org/10.1016/S0963-8695(99)00020-1

Molodova, M., Li, Z., Núñez, A., & Dollevoet, R. (2014). Automatic detection of squats in railway infrastructure. *IEEE Transactions on Intelligent Transportation Systems*, *15*(5), 1980–1990. https://doi.org/10.1109/TITS.2014.2307955

Molodova, M., Oregui, M., Núñez, A., Li, Z., & Dollevoet, R. (2016). Health condition monitoring of insulated joints based on axle box acceleration measurements. *Engineering Structures*, *123*, 225–235. https://doi.org/https://doi.org/10.1016/j.engstruct.2016.05.018

Pålsson, B. A., & Nielsen, J. C. (2012). Wheel–rail interaction and damage in switches and crossings. *Vehicle System Dynamics*, *50*(1), 43–58. https://doi.org/10.1080/00423114.2011.560673

ProRail. (2018). *Punt- en kruisstukken 54E1, Bewerking punt* (TKG412778).

ProRail. (2020). *Overzichtstekening GW 54E1 R195 1:9 Links voegloos op betonnen wisselliggers* (TKG420116).

ProRail. (2021). *Annual report 2021*. https://www.jaarverslagprorail.nl

Rytter, A. (1993). *Vibrational based inspection of civil engineering structures* (Doctoral dissertation No. 44). Denmark, Dept. of Building Technology; Structural Engineering, Aalborg University.

Shannon, C. (1949). Communication in the presence of noise. *Proceedings of the IRE*, *37*(1), 10–21. https://doi.org/10.1109/jrproc.1949.232969

Shevtsov, I. (2023). *Puntstukken en US handmetingen* (tech. rep.). ProRail.

Steenbergen, M. J. M. M. (2008). *Wheel-rail interaction at short-wave irregularities* (Doctoral dissertation). Delft University of Technology. http://resolver.tudelft.nl/uuid:98a5de70-3464-4487-b2c0-e4bfd51fac40

Torstensson, P., Squicciarini, G., Krüger, M., Pålsson, B., Nielsen, J., & Thompson, D. (2019). Wheel–rail impact loads and noise generated at railway crossings – influence of vehicle speed and crossing dip angle. *Journal of Sound and Vibration*, *456*, 119–136. https://doi.org/https://doi.org/10.1016/j.jsv.2019.04.034

Viechtbauer, C., Schagerl, M., & Schröder, K.-U. (2013). From NDT over SHM to SHC: The future for wind turbines. *6th International Conference on Structural Health Monitoring of Intelligent Infrastructure; Hong Kong December 2013*. https://publications.rwth-aachen.de/record/224986

VI-grade GmbH. (2022). *VI-Rail 2022.1 Documentation* (tech. rep.).

Wan, C. (2016). *Optimisation of vehicle-track interaction at railway crossings* (Doctoral dissertation). Delft University of Technology. https://doi.org/10.4233/UUID:8DAC8F02-FE9E-4BAA-9503-E9B3D79DD1AA

Wegdam, J. (2018). *Assessing crossing geometry: Expert tool for numerical & experimental assessment of turnout crossing geometry* (Master's thesis). Delft University of Technology. http://resolver.tudelft.nl/uuid:4505c798-0446-47b0-862f-19fd8632c8f7

Wegdam, J. (2021). *Assessing crossing degradation* (Master's thesis). Delft University of Technology. http://resolver.tudelft.nl/uuid:0107eff6-1d41-4f84-960e-a4e149c4b913

Wei, Z. (2018). *Modelling and monitoring of dynamic wheel-rail interaction at railway crossing* (Doctoral dissertation). Delft University of Technology. https://doi.org/10.4233/UUID:2DA90B9E-794E-45AC-AE72-0B532E058983

Wei, Z., Núnez, A., Li, Z., & Dollevoet, R. (2017). Evaluating Degradation at Railway Crossings Using Axle Box Acceleration Measurements. *Sensors*, *17*(10), 2236. https://doi.org/10.3390/s17102236

A

Multi-body dynamics simulation

A.1. Vehicle-track interaction

To confirm that the impact angle represents a lateral displaced wheelset is related to contact scenarios (as seen in Figure 2.4) a vehicle-track Multi-Body System (MBS) model is used. The software VI-Rail is used. It contains three sub-models that interact via each other via interfaces. First, the rolling stock is represented by a vehicle model. Relevant parameters like bogie and car body masses are defined, and the characteristics of their coupling via the primary and secondary suspension systems are set. Second, the track model represents the track. The geometry (straight track, curves, crossings, etc) is defined, along with relevant characteristics like rail profile, sleeper spacing, stiffness and damping. Lastly, the former two models are coupled to each other via a contact model. This models the actual interaction between vehicle and track. The three models are visualised in Figure A.1. In the following sections, each model is separately elaborated.

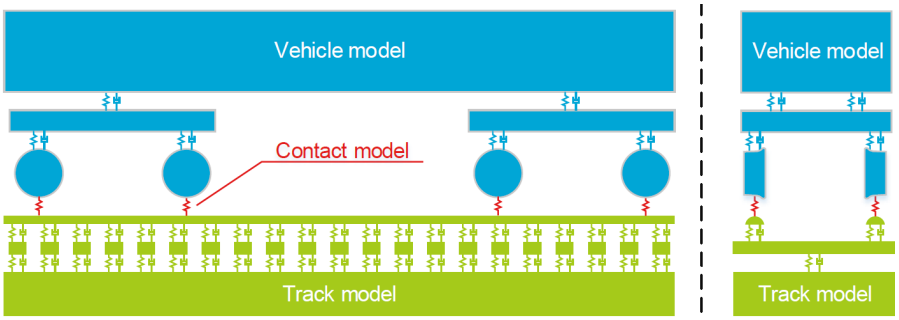

Figure A.1: A visualisation of the multi-body vehicle-track model. Adapted from Wegdam, 2018.

A.2. Vehicle model

In this thesis, the default VI-Rail model is taken as a starting point. This is the so-called Manchester Passenger Wagon, which is used as a simulation benchmark in the railway industry. Given that the ABA measurements are conducted with a very different type of train, the model is altered to simulate the used intercity's from NS. Specific values for e.g. spring stiffness and damping curves are based upon data from the former rolling stock maintainer of NS called Nedtrain. Geometrical properties (e.g. car body length) are based on technical drawings.

A.3. Track model

VI-Rail offers many customisation options to model the track. Generally the model is composed of three elements: the structure (geometry and properties), rail cross-section(s) and irregularities. The layout with an alignment irregularity and the track properties are found in Figure A.3 and Figure A.4 respectively. The output from the leading axle is considered, which is positioned at starting position x^*.

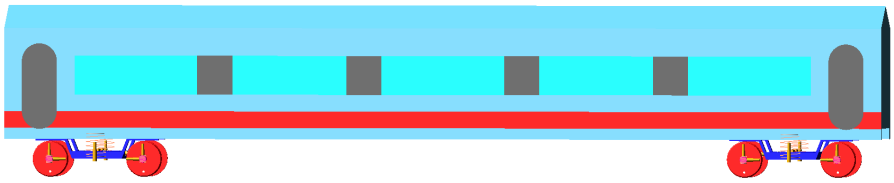

Figure A.2: The Manchester vehicle model from VI Rail. Adapted from Wegdam, 2018.

To simulate the effect of a laterally displaced wheelset, the track model with a short-wave horizontal alignment irregularity is introduced at in proximity of TP. This specific model is chosen to specifically study the effect of relative lateral displacement of the wheelset with respect to the crossing nose. This irregularity is unrealistic but effectively eliminates other variables that are dependent on e.g. vehicle properties or speed. The geometry is defined by cross-sections, which are based upon the nominal geometry as defined by ProRail, 2020.

Figure A.3: The track model layout with a short-wave alignment irregularity at close to TP. Adapted from Wegdam, 2018.

Rail mass:	54,77 kg/m	Flexible section initiation:	30 m
Ballast, lateral stiffness:	$45 \cdot 10^9$	Flexible section end:	36 m
Ballast, lateral damping:	$32 \cdot 10^3$	End of track:	150 m
Ballast, vertical stiffness:	$45 \cdot 10^9$	Sleeper distance:	0,6 m
Ballast, vertical damping:	$32 \cdot 10^3$	Sleeper height:	0,2 m
Ballast, rolling stiffness:	$10 \cdot 10^6$	Sleeper width:	0,3 m
Ballast, rolling damping:	$10 \cdot 10^3$	Rail height:	0,159 m
Rail pad, lateral stiffness:	$280 \cdot 10^6$	Rail I_{xx}:	$1{,}850 \cdot 10^{-5}\ m^4$
Rail pad, lateral damping:	$58 \cdot 10^3$	Rail I_{yy}:	$2{,}338 \cdot 10^{-5}\ m^4$
Rail pad, verical stiffness:	$1300 \cdot 10^6$	Rail I_{zz}:	$2{,}787 \cdot 10^{-6}\ m^4$
Rail pad, vertical damping:	$45 \cdot 10^3$	Rail area (cross-section):	$6{,}977 \cdot 10^{-3}\ m^2$
Rail pad, rolling stiffness:	$360 \cdot 10^6$	Young's modulus:	$2{,}1 \cdot 10^{11}$
Rail pad, rolling damping:	$360 \cdot 10^3$	Rail damping ratio:	$1{,}0 \cdot 10^{-4}$

Figure A.4: Track model properties. Adapted from Wegdam, 2018.

A.4. Contact model

VI-Rail provides three contact models via a wheel-rail element. The wheel-rail element describes the kinematics of one wheel relative to one rail. The available elements are WRTAB, WRQLT and WRGEN (VI-grade GmbH, 2022). WRTAB uses pre-calculated non-linear kinematic functions as input (stored as tabular values, hence the abbreviation). The actual wheel and rail profile are considered but the contact patch is approximated by an ellipse. WRQLT is a quasi-linear element with kinematics described by conicity, contact angle and roll angle. Circular profiles for the wheel and rail are constructed based on these values. The actual wheel and (local) rail profiles are therefore not used. The WRGEN element uses the wheel and rail profile as input and computes the actual contact kinematics in each simulations step. It allows for multiple contact points and evaluates local contact stiffness besed on geometry, loading and material properties. This gives the most accurate description of the wheel-rail contact but is the most computationally heavy. The WRGEN contact element is chosen to be used in this thesis.

A.5. Results

The time step per iteration is set to 0.001 s. This enables to capture the impact at a sufficient high frequency without getting an oscillating solution due to the geometrical interpolation in between discrete cross-sections. The result of a single simulation is seen in Figure A.5. The dots represent the impact values that are considered. The impact angle is calculated manually from these results. Two extreme scenarios are considered: no lateral displacement and 6mm relative displacement towards the crossing nose. Four different speeds are simulated to quantify the speed dependence. The impacts in vertical and lateral direction from all simulations are seen in Figure A.6a and Figure A.6b. The resultant impact angle is seen in Figure A.6c.

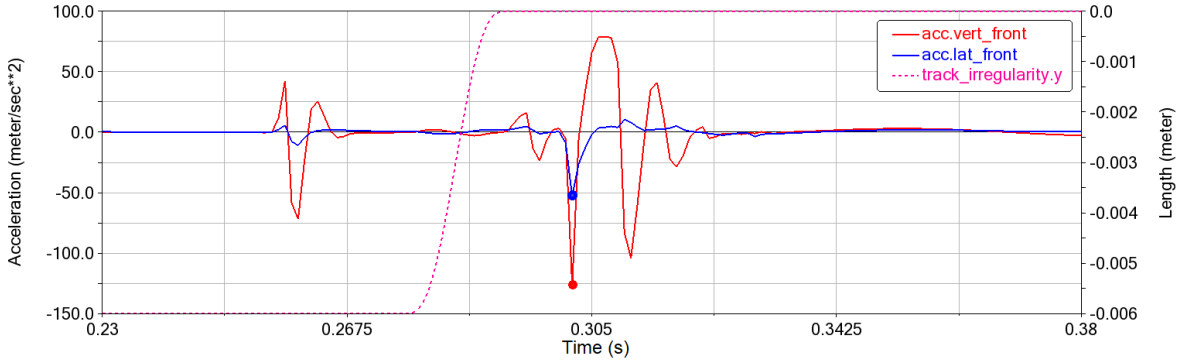

Figure A.5: ABA of a single simulation at 27.77 m/s (100 km/h) with an alignment irregularity. The dots indicate the impacts.

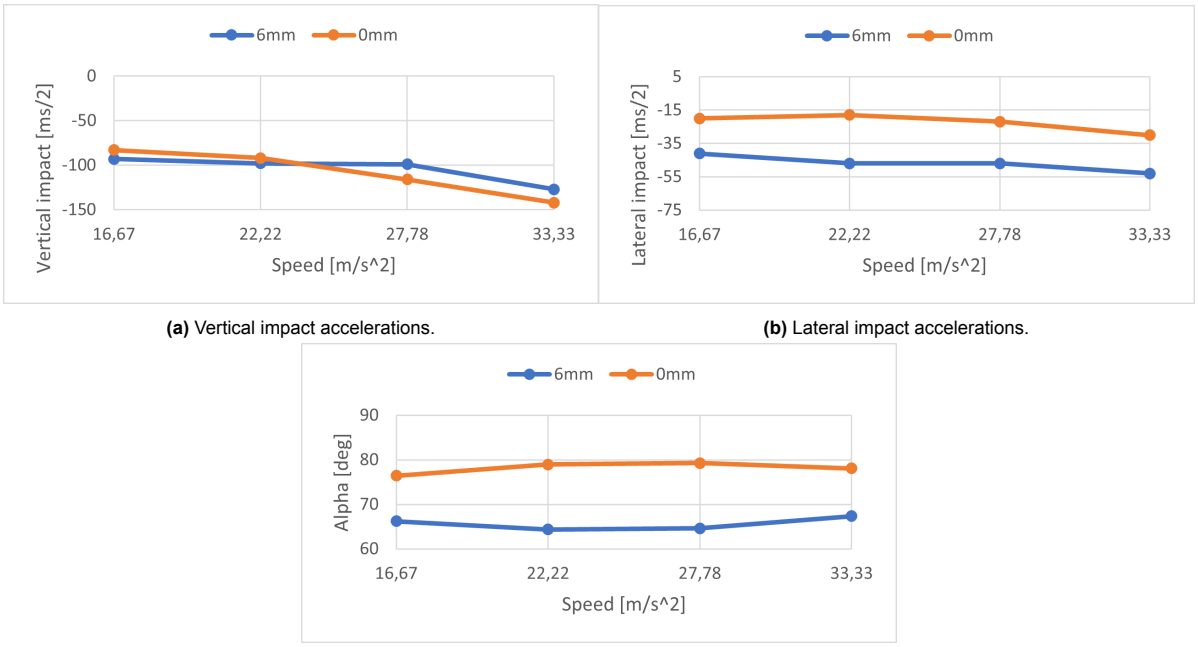

(a) Vertical impact accelerations.

(b) Lateral impact accelerations.

(c) Resultant impact angle.

Figure A.6: Results of multiple MBS simulations with varying speed and irregularity.

As expected from Section 2.2.3, the vertical impact amplitude increases almost linear with increasing speed. The lateral displaced wheelset does not influence the vertical impact amplitude much. The lateral impacts seem to also scale linear with speed. The lateral displaced wheelset shows a twice higher lateral impact amplitude while still scaling similar as the non-displaced wheelset with respect to speed. Lastly, the impact angle is almost almost constant with respect to speed. The non-displaced wheelset has a dominant vertical component. The displaced wheelset however has a much more significant lateral component, showing a significant smaller impact angle.

B

Geometry data processing

B.1. Laser measurement data

The geometry of turnouts in The Netherlands is measured by dedicated turnout geometry measurement trains using laser scanners. While driving over a turnout, the outline of the turnout is captured a discrete intervals resulting in a dataset consisting of a point cloud. The supplier checks, localises and calibrate the measurement data and delivers it in a predefined format which is compliant with the prescribed standards. Wegdam, 2021 created a post-processing analysis method to determine relevant condition parameters like wear levels and kinematic wheel dip based upon this data. The analysis output of his method is utilised in this thesis as validation for the assessment method in Chapter 4.

Wear levels are determined by identifying the difference between the original geometry fitted to each cross-section, the wheel dip is determined by letting a single nominal S1002 wheel pass virtually over the centre trajectory of the measured geometry. For an in-depth elaboration of the inner workings, see Wegdam, 2021. A visualisation of the analysis output of a single cross-section is show in Figure B.1. The longitudinal variance of these per cross-section parameters is seen in Figures B.2a and B.2b.

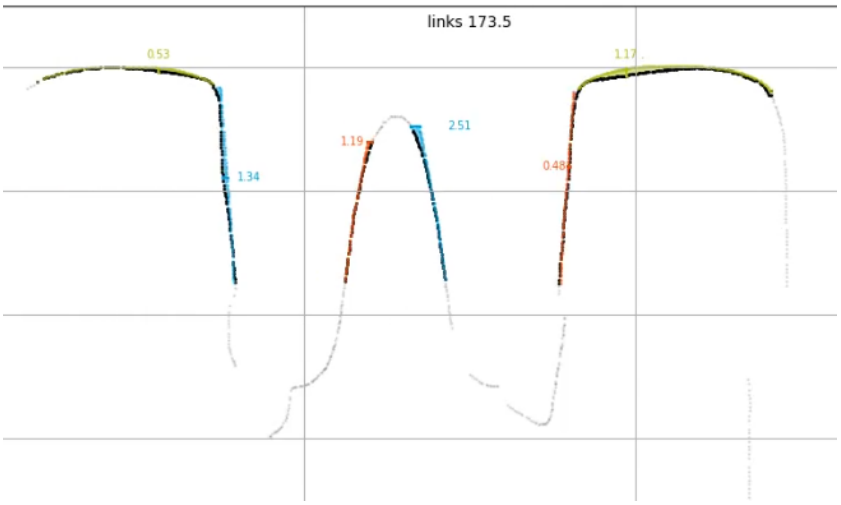

Figure B.1: A close up of the visualisation of the geometry analysis output at a single cross-section. The grey dots represent the processed laser scanned outline of the turnout. The coloured lines and values correspond to deviating geometry with respect to the original drawings indicating wear.

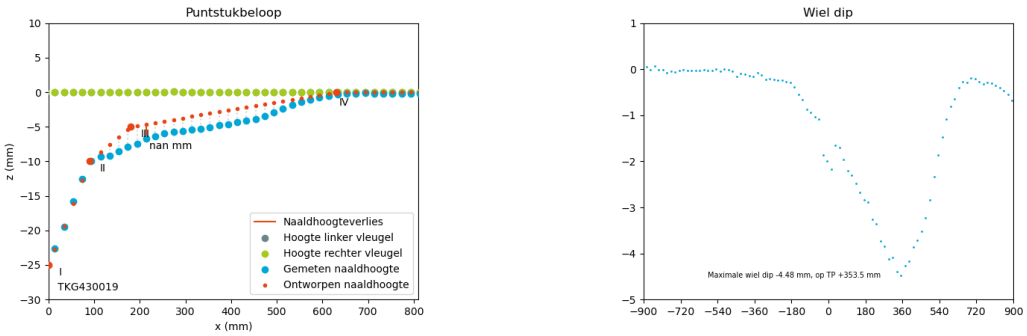

(a) Longitudinal-vertical profile of the crossing.

(b) Kinematic wheel dip of the centre trajectory.

Figure B.2: Longitudinal analysis outputs.

B.2. Signal denoising

The raw geometry data and some of the analysis output are noisy, like (parts of) the wheel dip trajectory in Figure B.2b or the lateral crossing nose wear in Figure B.3a. There are large spikes due to measurement errors and lack of filtering. To estimate the local wear, a two-stage filtering chain is applied. First, large unrealistic values (spikes) with thresholds as defined in Table B.1. Secondly, the de-spiked signal is smoothed by a Gaussian filter with a standard deviation of 2 data points. This effectively filters out the spikes and high-frequency content (large fluctuations) and leaves the 'trend'. This is translates the data into a usable form and provides sufficient precision for the intended purpose of estimating the lateral wear level on the crossing nose. The lateral wear level of the crossing nose is defined as the maximum of the denoised signal between 300 mm and 600 mm.

Table B.1: Thresholds for dropping individual data points.

Parameter	Threshold
Lateral wear crossing nose	>15 mm
Lateral wear wing rail	>10 mm
Wheel dip displacement	>5 mm

B.3. Condition estimators

The condition of a crossing is hard to captured by a single line, or value. It also depends on the definition of what a good or bad condition is. However, certain parameters can given an indication or estimation of favourable or unfavourable track-crossing interaction. As elaborated in Section 2.2.3, the kinematic wheel dip angle could serve as estimator for the vertical impacts on the crossing nose. Lateral wear levels on the crossing nose or wing rail indicate a frequent occurrence of irregular contact (see Figure 2.4). Therefore, to validate the proposed method in Chapter 4, structural health indicators are derived from the processed and filtered geometry laser measurements: lateral crossing nose wear, lateral wing rail wear and the wheel dip angle.

The lateral crossing nose wear generally has a distinct peak between 300 mm and 600 mm, which corresponds with the expected location of impact on the crossing nose. The crossing nose's wear level is defined as the maximum of the peak in this interval. The lateral wing rail wear shows similarities with a bi-linear curve. From -400 mm to 0 mm, the wear can be approximated by a linear positive function. From 0 mm up to 800 mm a slightly declining linear plateau can be identified. The lateral wing rail wear level is defined as the maximum wear, located from -100mm to 200 mm. The wheel dip angle can be derived from the kinematic wheel trajectory and is defined as seen in Figure 2.9. The angle is calculated from the intersection of two linear approximations of the wheel dip. It was not a goal of this thesis to derive an algorithm for automatic dip angle estimation, therefore the linear approximations are based upon manual selection of data points. The linearisation is done based upon data points just above the 'round part' of the dip bottom and a data point 10% higher. This approach is sufficiently accurate for the estimation purpose. However, it makes this metric not fully objective.

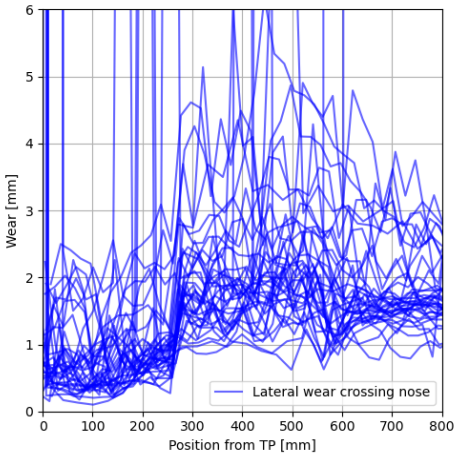

(a) Noisy lateral crossing nose wear.

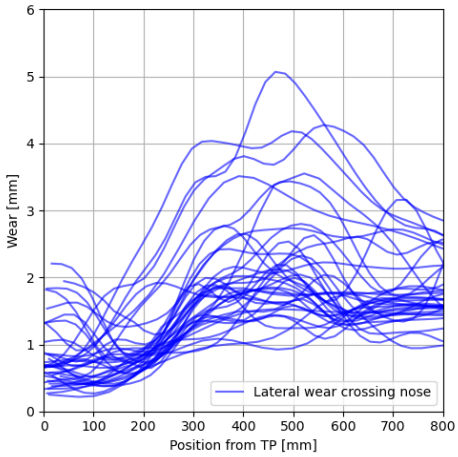

(b) Denoised lateral crossing nose wear.

Figure B.3: Lateral wear on the crossing nose prior and after denoising by dropping outliers and applying a Gaussian filter.

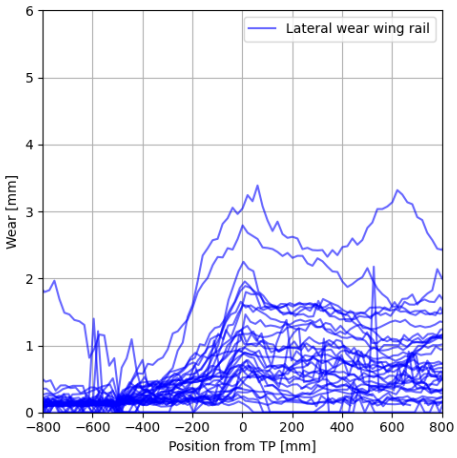

(a) Noisy lateral wear of wing rails.

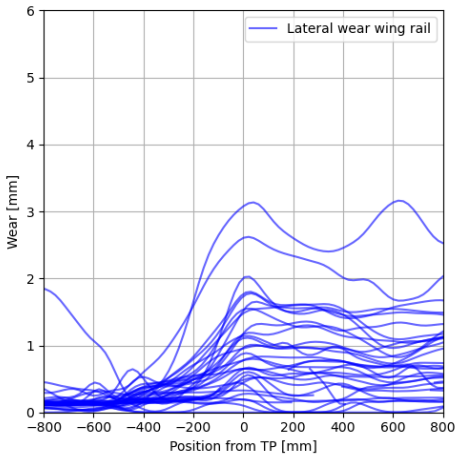

(b) Denoised lateral wing rail wear.

Figure B.4: Wing rail wear prior and after denoising by applying a Gaussian filter.

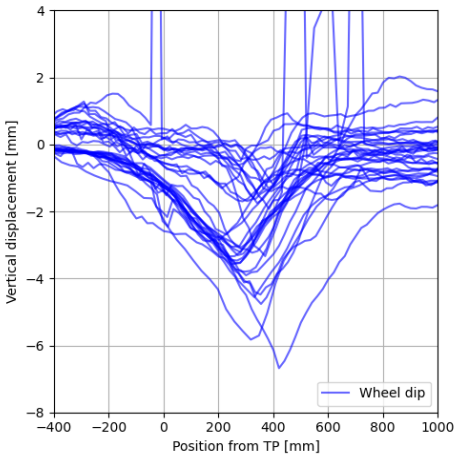

(a) Noisy wheel dip trajectories.

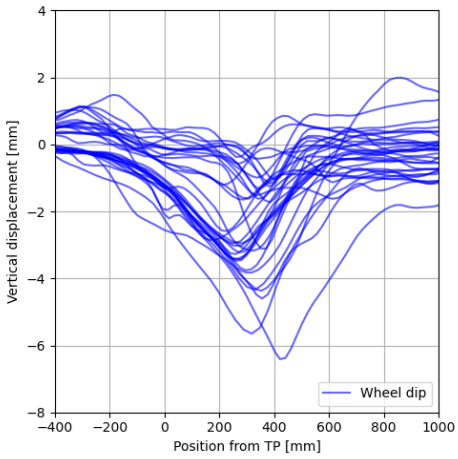

(b) Denoised wheel dip trajectories

Figure B.5: Wheel dip trajectories prior and after denoising by dropping outliers and applying a Gaussian filter.